ICES REPORT 10-05

March 2010

An Isogeometric Approach To Cohesive Zone Modeling

by

Clemens Verhoosel, Michael Scott, Rene de Borst,
and Thomas Hughes

The Institute for Computational Engineering and Sciences
The University of Texas at Austin
Austin, Texas 78712

INTERNATIONAL JOURNAL FOR NUMERICAL METHODS IN ENGINEERING
Int. J. Numer. Meth. Engng 2000; **00**:1–30 *Prepared using* `nmeauth.cls` *[Version: 2002/09/18 v2.02]*

An isogeometric approach to cohesive zone modeling

Clemens V. Verhoosel[1,2*], Michael A. Scott[2], René de Borst[1] and Thomas J. R. Hughes[2]

[1] *Department of Mechanical Engineering, Eindhoven University of Technology, 5600 MB, Eindhoven, The Netherlands*
[2] *Institute for Compuational Engineering and Sciences, University of Texas at Austin, 78712, Austin, Texas, U.S.A.*

SUMMARY

The possibility of enhancing a B-spline basis with discontinuities by means of knot insertion makes isogeometric finite elements a suitable candidate for modeling discrete cracks. In this contribution we use isogeometric finite elements to discretize the cohesive zone formulation for failure in materials. In the case of a pre-defined interface, non-uniform rational B-splines (NURBS) are used to obtain an efficient discretization. In the case that propagating cracks are considered, T-splines are found to be more suitable, due to their ability to generate localized discontinuities. Various numerical simulations demonstrate the suitability of the isogeometric approach to cohesive zone modeling. Copyright © 2000 John Wiley & Sons, Ltd.

KEY WORDS: Fracture, Cohesive zone models, Isogeometric analysis, NURBS, T-splines

1. INTRODUCTION

Understanding and predicting failure is of crucial importance for improving the design of many engineering structures. Failure of materials is characterized by the appearance of discrete cracks. In contrast to purely brittle fracture, the failure process in most materials takes place in a zone that is larger than its atomistic microstructure. A realistic description of failure requires this process zone to be taken into account.

Discrete fracture models that incorporate a process zone, referred to as cohesive zone models, were introduced by Dugdale [1] and Barenblatt [2]. In contrast to the models for brittle fracture, as introduced by Griffith [3], in a cohesive zone model a material gradually loses its load-bearing capacity. The finite element method is commonly used for the discretization of cohesive zone models. From the perspective of element technology, the challenge lies in flexibly capturing the internal traction boundaries, by which cracks are modeled. This is particularly so when propagating discontinuities are to be simulated. Among the available finite element

---

*Correspondence to: `c.v.verhoosel@tue.nl`, Department of Mechanical Engineering, Eindhoven University of Technology, 5600 MB, Eindhoven, The Netherlands

technologies for capturing propagating discontinuities are interface elements (e.g. [4, 5, 6]) and embedded discontinuities (e.g. [7, 8]). Nowadays, the partition of unity method (PUM, or XFEM, e.g. [9, 10, 11]) is considered as the most flexible element technology for capturing propagating cracks.

In this contribution isogeometric finite elements, as introduced by Hughes et al. [12], are used to introduce the cohesive zone. Isogeometric analysis is regarded as the fusion of computer aided design (CAD) and finite element analyses (FEA), and has successfully been applied to a large variety of problems [13], including problems in solid mechanics (e.g. [12, 14, 15]). Isogeometric finite elements have several advantages compared to classical finite elements. Their ability to exactly represent complex geometries is of particular interest in cohesive zone models, since the mesh resolution in such models is often dictated by the necessity to capture complex geometries (e.g. hard inclusions embedded in a softer matrix). Another advantage of isogeometric finite elements is the higher-order continuity conditions that can be achieved. In cohesive zone models, this is important since cracks can be discretized by smooth surfaces.

One possibility of discretizing the cohesive zone formulation using isogeometric finite elements is to use them in combination with the partition of unity method. In that case the discontinuities would be embedded in the solution space by means of Heaviside functions. Although such an approach would benefit from both advantages of the isogeometric approach, isogeometric finite elements offer the possibility to directly insert discontinuities in the solutions space. The conceptual idea is that in the isogeometric approach the inter-element continuity can be decreased by means of knot insertion, e.g. [16]. Knots should not be confused with finite element nodes, although the proposed concept of treating discontinuities is similar to that in interface elements.

In this contribution we show that the isogeometric concept can be used to discretize both pre-defined and propagating discontinuities. In section 2 we introduce the cohesive zone formulation along with the fundamental set of assumptions made in this work. In section 3 we introduce the isogeometric discretization strategy. We first discuss how discontinuities can be inserted in B-splines and NURBS, the fundamental building blocks of isogeometric analysis. Subsequently, we outline how discontinuity boundaries can be inserted in NURBS and T-splines, which are used for modeling pre-defined and propagating discontinuities, respectively. In section 4 we discuss some algorithmic aspects, and the approach is demonstrated by a variety of numerical simulations in section 5.

2. COHESIVE ZONE FORMULATION

Consider a solid $\Omega \subset \mathbb{R}^N$ (with $N = 2$ or 3) as shown in Figure 1. The displacement of the material points $x \in \Omega$ is described by the displacement field $u \in \mathbb{R}^N$. The external boundary of the body is composed of a boundary Γ_u on which essential boundary conditions are provided, and a boundary Γ_t with natural boundary conditions. In addition an internal boundary Γ_{d} is present which represents either an adhesive interface between two separate regions, or a cohesive crack.

Under the assumption of small displacements and displacement gradients, the deformation of the material is characterized by the infinitesimal strain tensor $\varepsilon_{ij} = \frac{1}{2}\left(\frac{\partial u_i}{\partial x_j} + \frac{\partial u_j}{\partial x_i}\right)$. Furthermore, the crack opening $[\![u_i]\!]$ is defined as the difference between the displacements

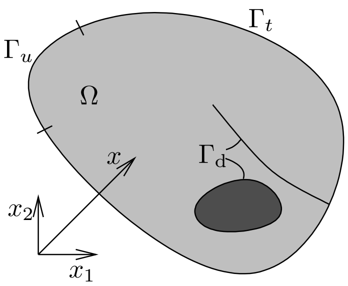

Figure 1. Schematic representation of a solid body Ω with internal discontinuity boundaries $\Gamma_{\rm d}$.

on either side of the internal discontinuity $\Gamma_{\rm d}$. In the absence of body forces, the strong form quasi-static equilibrium equations are then given by

$$\begin{cases} \frac{\partial \sigma_{ij}}{\partial x_j} = 0 & x \in \Omega \\ u = \hat{u} & x \in \Gamma_u \\ \sigma_{ij} n_j = \hat{t}_i & x \in \Gamma_t \\ \sigma_{ij} n_j = t_i(\llbracket u \rrbracket) & x \in \Gamma_{\rm d} \end{cases} \tag{1}$$

In these equations σ is the Cauchy stress tensor and n is the vector normal to the boundaries. The prescribed boundary displacements and traction are given by $\hat{u}$ and $\hat{t}$, respectively, and the Einstein summation convention has been used.

The weak form of the equilibrium equations (1) is obtained by multiplication with a virtual displacement δu and integrating over the domain Ω. After the application of Gauss' theorem, this results in

$$\int_\Omega \sigma_{ij} \delta\varepsilon_{ij} \, {\rm d}\Omega + \int_{\Gamma_{\rm d}} t_i \delta \llbracket u_i \rrbracket \, {\rm d}\Gamma_{\rm d} = \int_{\Gamma_t} \hat{t}_i \delta u_i \, {\rm d}\Gamma_u \tag{2}$$

This equation should be satisfied for any admissible displacement field δu subject to the Dirichlet boundary conditions on Γ_u. The Dirichlet boundary conditions are satisfied by building them into the solution space. From an implementation point of view, it is convenient to rewrite the weak form, equation (2), in matrix-vector notation as

$$\int_\Omega \boldsymbol{\sigma}^{\rm T} \delta\boldsymbol{\gamma} \, {\rm d}\Omega + \int_{\Gamma_{\rm d}} \mathbf{t}^{\rm T} \delta \llbracket \mathbf{u} \rrbracket \, {\rm d}\Gamma_{\rm d} = \int_{\Gamma_t} \hat{\mathbf{t}}^{\rm T} \delta \mathbf{u} \, {\rm d}\Gamma_u \tag{3}$$

where $\boldsymbol{\sigma}$ and $\boldsymbol{\gamma}$ are the Voigt form of the Cauchy stress tensor σ and engineering strain, respectively. Matrix-vector notation will be used in the remainder of this work, with bold fonts indicating matrices and vectors.

The essence of the cohesive zone formulation is the relation between the traction acting on $\Gamma_{\rm d}$ and the jump in the displacement field over this internal boundary, as represented by the last equation of (1) and the second integral in the equations (2) and (3). The relation $\mathbf{t} = \mathbf{t}(\llbracket \mathbf{u} \rrbracket)$ is commonly referred to as the traction-opening relation, or the cohesive law. Generally a distinction is made between initially rigid and initially elastic traction-opening relations. The former case is typical for cohesive cracks, for which the discontinuity only appears when a fracture criterion is violated. The latter is typical for adhesive cracks, which show a gradual increase in opening before their fracture strength is reached, after which unrecoverable damage accumulates in the interface. Over the past decades many different traction-opening relations have been proposed for a wide variety of applications. The two most important parameters used in these models are the fracture strength, which is the maximum traction that can be applied on an interface, and the fracture toughness, which represents the amount of energy dissipated per unit of cracked surface.

In many cases one is interested in studying the evolution of cracks, and their effect on the load bearing capacity of a structure. In those cases, the internal discontinuity boundary Γ_{d} gradually extends through the domain Ω in such a way that $\Gamma_{\mathrm{d}}(t) \subseteq \Gamma_{\mathrm{d}}(t+\Delta t)$. The evolution of the discontinuity is governed by a fracture criterion, which requires the stress state at the crack tip to be equal to the fracture strength when the crack is propagating. The direction of propagation is usually taken perpendicular to that of the maximum principal stress.

Here we apply a staggered solution procedure to model the evolution of the discontinuity boundary, as is also commonly done in partition of unity-based approaches (e.g. [9, 11]) and interface elements-based approaches (e.g. [17]). In this staggered approach we solve the equilibrium equations (3) for a fixed internal boundary Γ_{d}. If the stresses are such that the fracture criterion inside the domain Ω is violated, we create a new discontinuity. We extend the crack with an increment that can depend on the employed discretization. A similar approach can be found in the context of configurational force models for fracture (e.g. [18]).

3. THE ISOGEOMETRIC APPROACH

The fundamental idea of the isogeometric approach is to discretize the cohesive zone formulation discussed in section 2 using a solution space that: i) exactly represents a broad range of geometric entities, and ii) allows for discontinuities in the displacement field over the internal boundaries Γ_{d}. We first demonstrate how discontinuities are introduced in B-splines and non-uniform rational B-splines (NURBS). These basis functions can be considered the fundamental building blocks of isogeometric analysis. We then demonstrate how NURBS can be used to model pre-defined discontinuities. Next, we introduce T-splines and demonstrate their superiority to NURBS when used to model propagating discontinuities.

3.1. Discontinuities in B-splines and NURBS

The fundamental building block of isogeometric analysis is the univariate B-spline, e.g. [16, 13]. A univariate B-spline is a piecewise polynomial defined over a knot vector $\Xi = \{\xi_1, \xi_2, \ldots, \xi_{n+p+1}\}$, with n and p denoting the number and order of basis functions, respectively. The knot values ξ_i are non-decreasing with increasing knot index i, i.e. $\xi_1 \leq \xi_2 \leq \ldots \leq \xi_{n+p+1}$. As a consequence, the knots divide the parametric domain $[\xi_1, \xi_{n+p+1}] \subset \mathbb{R}$ in knot intervals of non-negative length. We refer to the knot intervals of positive length as elements. When several knot values coincide, their multiplicity is indicated by m_i, where i corresponds to the index of the knot values. The B-splines used for analysis purposes are generally open B-splines, which means that the multiplicity of the first and last knot (m_1 and m_{n+p+1}) is equal to $p+1$.

A B-spline of order p is defined as a linear combination of n B-spline basis functions

$$a(\xi) = \sum_{i=1}^{n} N_{i,p}(\xi) A_i \tag{4}$$

where $N_{i,p}(\xi)$ represents a B-spline basis function of order p and A_i is called a control point or variable. Equation (4) is typically used for the parameterization of curves in two (with $A_i \in \mathbb{R}^2$) or three (with $A_i \in \mathbb{R}^3$) dimensions. For open B-splines $a(\xi_1) = A_1$ and $a(\xi_{n+p+1}) = A_n$.

The B-spline basis is defined recursively, starting with the zeroth order ($p = 0$) functions

$$N_{i,0}(\xi) = \begin{cases} 1 & \xi_i \leq \xi < \xi_{i+1} \\ 0 & \text{otherwise} \end{cases} \tag{5}$$

from which the higher-order ($p = 1, 2, \ldots$) basis functions follow by the Cox-de Boor recursion formula [19, 20]

$$N_{i,p}(\xi) = \frac{\xi - \xi_i}{\xi_{i+p} - \xi_i} N_{i,p-1}(\xi) + \frac{\xi_{i+p+1} - \xi}{\xi_{i+p+1} - \xi_{i+1}} N_{i+1,p-1}(\xi) \tag{6}$$

Efficient and robust algorithms exist for the evaluation of these non-negative basis functions and their derivatives, e.g. [21]. B-spline basis functions satisfy the partition of unity property, and B-spline parameterizations possess the variation diminishing property, e.g. [22]. B-splines are also refineable, which is important in the context of isogeometric analysis, e.g. [23]. However, a drawback of B-splines is their inability to exactly represent many objects of engineering interest, such as conic sections. For this reason NURBS, which are a rational generalization of B-splines, are commonly used. A NURBS is defined as

$$a(\xi) = \sum_{i=1}^{n} \frac{N_{i,p}(\xi) W_i}{w(\xi)} A_i = \sum_{i=1}^{n} R_{i,p}(\xi) A_i \tag{7}$$

where $w(\xi) = \sum_{i=1}^{n} N_{i,p}(\xi) W_i$ is the weighting function. In the special case that $W_i = c \; \forall i$, where c may be an arbitrary constant, the NURBS basis reduces to the B-spline basis.

In this contribution, the NURBS (or B-spline) basis is used for both the parameterization of the geometry and the approximation of the solution space for the displacement field u, that is

$$x(\xi) = \sum_{i=1}^{n} R_{i,p}(\xi) X_i \tag{8}$$

$$u(\xi) = \sum_{i=1}^{n} R_{i,p}(\xi) U_i \tag{9}$$

We refer to X_i and U_i as the control points and displacement control variables, respectively. In contrast to C^0 finite elements, a control point or variable does not generally coincide with an element vertex in the physical space.

The property of NURBS of particular interest for cohesive zone modeling is that they are $p - m_i$ times continuously differentiable over a knot i. This allows for the direct discretization of higher-order differential equations, e.g. [24]. The ability to control inter-element continuity is useful for cohesive zone models, since discontinuities can be inserted arbitrarily by means of

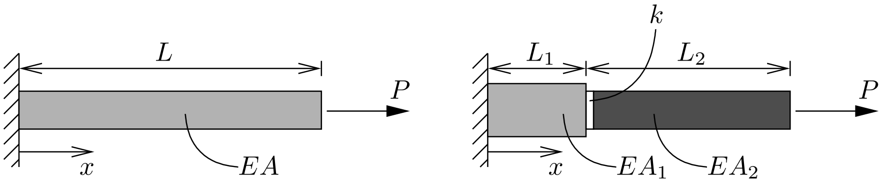

Figure 2. Schematic representation of two rods loaded in tension. The two segments of the composite rod are connected by a zero thickness adhesive layer with stiffness k.

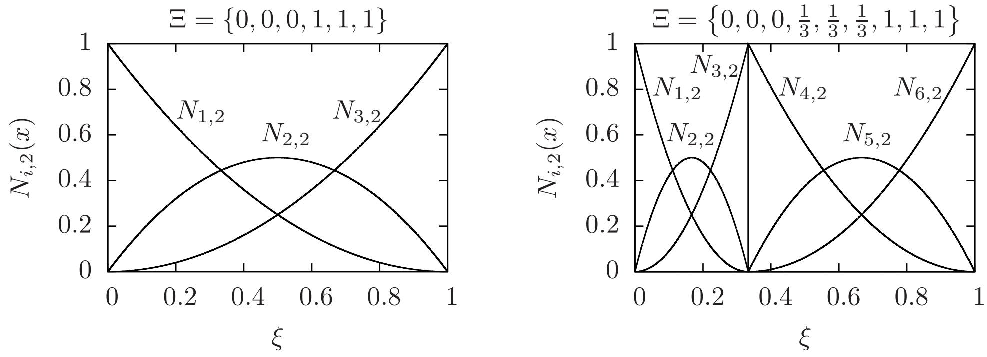
$\Xi = \{0, 0, 0, 1, 1, 1\}$

$\Xi = \left\{0, 0, 0, \frac{1}{3}, \frac{1}{3}, \frac{1}{3}, 1, 1, 1\right\}$

Figure 3. Quadratic B-spline basis functions used for the one-dimensional rod example without (left) and with (right) a discontinuity at $x_{\mathrm{d}} = L_1 = \frac{1}{3}L$.

knot insertion. In fact, a jump in the displacement field at a certain point $x_{\mathrm{d}} = x(\xi_{\mathrm{d}})$ in the physical space can be created by raising the multiplicity of the knot ξ_{d} to $m_i = p + 1$. There exist efficient methods to determine parametric position ξ_{d} from x_{d}. In general, a non-linear iterative procedure is required [21].

We illustrate the concept of inserting discontinuities in the solution space by means of a simple example, viz. a one-dimensional rod loaded in tension (Figure 2). The rod has length L, stiffness EA and is loaded by a force P. Let the rod be parameterized by a quadratic NURBS with knot vector $\Xi = \{0, 0, 0, 1, 1, 1\}$, and let the control points be given by $X_1 = 0$, $X_2 = \frac{1}{2}L$ and $X_3 = L$ with uniform weigths $W_1 = W_2 = W_3 = 1$. The corresponding basis functions are shown in Figure 3. This choice of control points results in a linear parameterization of the rod, i.e. $x = L\xi$. Using the shape functions, the displacement field can be approximated by equation (9). Any convenient method for solving this problem will then give the coefficients $U_1 = 0$, $U_2 = \frac{1}{2}\frac{PL}{EA}$ and $U_3 = \frac{PL}{EA}$, so that $u(\xi) = \frac{PL\xi}{EA}$, which can obviously be rewritten as the exact solution $u(x) = \frac{Px}{EA}$.

Now consider the composite rod shown in the right of Figure 2. The two segments of the rod, with stiffnesses EA_1 and EA_2 and lengths L_1 and L_2 (with $L_1 + L_2 = L$), are connected by an adhesive layer at $x = L_1$. The (zero thickness) adhesive layer is assumed to have a stiffness k, such that the displacement jump over the layer equals $[\![u]\!] = P/k$. Since the basis functions corresponding to $\Xi = \{0, 0, 0, 1, 1, 1\}$ are C^1-continuous on $(0, L)$, the discontinuous deformation of the composite rod cannot be represented exactly by these basis functions.

In order to be able to find the exact solution of the composite rod problem, we enhance the solution space by allowing for a discontinuity in the displacement field at $x_\mathrm{d} = L_1$. From the parameterization of the rod we know that this physical position coincides with the point $\xi_\mathrm{d} = \frac{L_1}{L}$ in the parametric domain. In order to create a discontinuity at $x_\mathrm{d} = L_1$ we insert a knot with multiplicity $p + 1 = 3$ at $\xi = \frac{L_1}{L}$, which changes the knot vector to $\Xi = \left\{0, 0, 0, \frac{L_1}{L}, \frac{L_1}{L}, \frac{L_1}{L}, 1, 1, 1\right\}$. The corresponding basis functions for the case that $L_1 = \frac{1}{3}L$ are shown in Figure 3. When the corresponding control points are taken as $X_1 = 0$, $X_2 = \frac{1}{2}L_1$, $X_3 = L_1$, $X_4 = L_1$, $X_5 = L_1 + \frac{1}{2}L_2$, $X_6 = L$, the original parameterization is preserved. If we then determine the deformation of the rod using the new basis functions, we find the coefficients $U_1 = 0$, $U_2 = \frac{1}{2}\frac{PL_1}{EA_1}$, $U_3 = \frac{PL_1}{EA_1}$, $U_4 = \frac{PL_1}{EA_1} + \frac{P}{k}$, $U_5 = \frac{PL_1}{EA_1} + \frac{P}{k} + \frac{1}{2}\frac{PL_2}{EA_2}$ and $U_6 = \frac{PL_1}{EA_1} + \frac{P}{k} + \frac{PL_2}{EA_2}$, which is the exact solution to the problem.

3.2. Discretization of a solid with pre-defined discontinuities using NURBS

The isogeometric concept introduced in the previous section can be extended to the multi-dimensional case. In the remainder of this work we restrict ourselves to the two-dimensional case. The parameterization of a body $\Omega \subset \mathbb{R}^2$ can then be obtained by a NURBS surface. Such a surface can be comprised of one or more NURBS patches. A two-dimensional NURBS patch gives a bivariate parameterization of Ω based on the knot vectors $\Xi = \{\xi_1, \xi_2, \ldots \xi_{n+p+1}\}$ and $\mathcal{H} = \{\eta_1, \eta_2, \ldots \eta_{s+t+1}\}$ (such that $(\xi, \eta) \in [\xi_1, \xi_{n+p+1}] \otimes [\eta_1, \eta_{s+t+1}] \subset \mathbb{R}^2$) as

$$\mathbf{x}(\xi, \eta) = \sum_{i=1}^{n} \sum_{j=1}^{s} R_{i,j}^{p,t}(\xi, \eta) \mathbf{X}_{i,j} \tag{10}$$

in which the bivariate NURBS basis functions are given by

$$R_{i,j}^{p,t}(\xi, \eta) = \frac{N_{i,p}(\xi) M_{j,t}(\eta) W_{i,j}}{\sum_{\imath=1}^{n} \sum_{\jmath=1}^{s} N_{\imath,p}(\xi) M_{\jmath,t}(\eta) W_{\imath,\jmath}} \tag{11}$$

where $N_{i,p}(\xi)$ and $M_{j,t}(\eta)$ are univariate B-spline basis functions defined over the knot vectors Ξ and $\mathcal{H}$, respectively. From equation (10) it is observed that an arbitrary body Ω can be parametrized by the provision of the nodal control points $\mathbf{X}_{i,j} \in \mathbb{R}^2$ and their corresponding weights $W_{i,j}$. We refer to the set of control point positions and weights as the control net. An example of the parameterization of a body Ω by a cubic ($p = t = 3$) NURBS patch is shown in the top pictures of Figure 4. A shaded area in the index space corresponds to a region of nonzero area in the parameter space. We call these shaded regions elements.

A body Ω with an internal discontinuity boundary Γ_d can also be parameterized by a single NURBS patch, as shown in the bottom pictures of Figure 4. In this case, the discontinuity is created by inserting a knot at $\eta = \eta_\mathrm{d} = \frac{1}{3}$ with multiplicity $t+1 = 4$ in the knot vector $\mathcal{H}$. In the case of the small deformation cohesive zone formulation, the continuity of the position vector $\mathbf{x}$ is preserved by constraining the control point positions (and their weights) on either side of the discontinuity. From an implementation point of view, those constraints are enforced by equating the positions and weights of the control point pairs on the crack surface. This constraint is not required in the case of the displacement field

$$\mathbf{u}(\xi, \eta) = \sum_{i=1}^{n} \sum_{j=1}^{s} R_{i,j}^{p,t}(\xi, \eta) \mathbf{U}_{i,j} \tag{12}$$

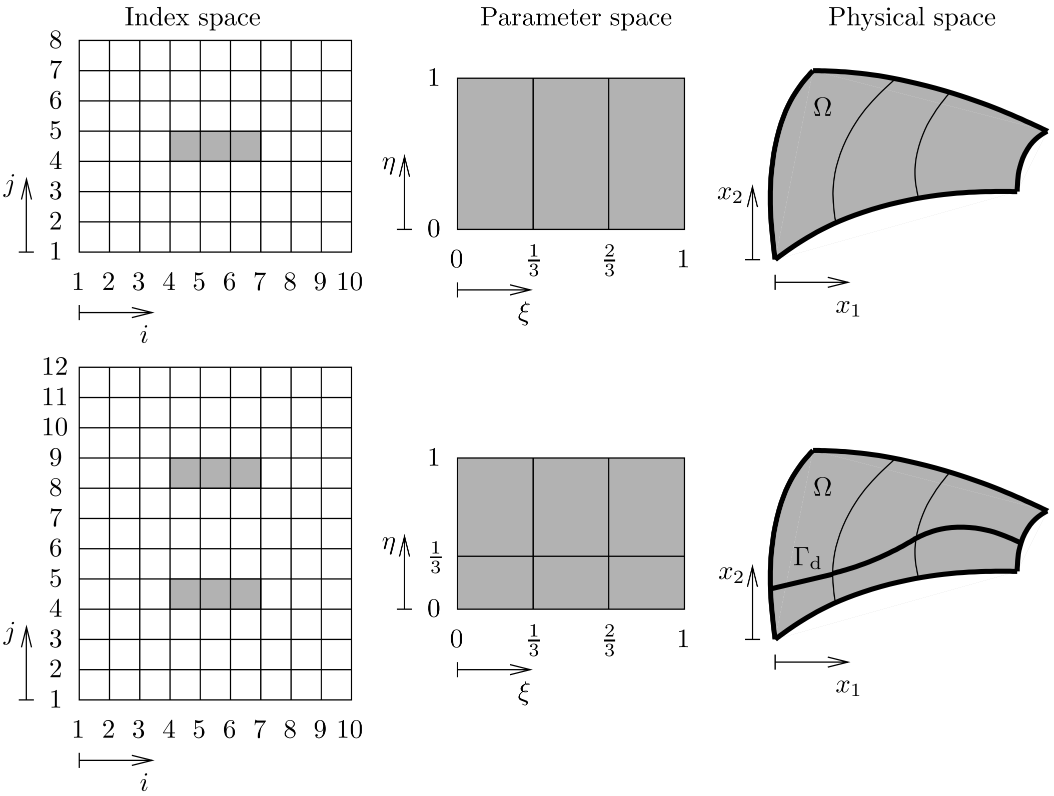

Figure 4. Index space, parameter space and physical space of a cubic NURBS patch without (top) and with (bottom) an internal discontinuity Γ_d. The knot vectors for the body without discontinuity are given by $\Xi = \left\{0,0,0,0,\frac{1}{3},\frac{2}{3},1,1,1,1\right\}$ and $\mathcal{H} = \left\{0,0,0,0,1,1,1,1\right\}$. For the body with internal boundary Γ_d the knot vectors are equal to $\Xi = \left\{0,0,0,0,\frac{1}{3},\frac{2}{3},1,1,1,1\right\}$ and $\mathcal{H} = \left\{0,0,0,0,\frac{1}{3},\frac{1}{3},\frac{1}{3},\frac{1}{3},1,1,1,1\right\}$.

Hence, a jump in the displacement field over the discontinuity boundary Γ_d can be captured by the solution space. Note that in a large deformations setting, the material position field $\mathbf{x}$ in the deformed configuration is discontinuous. In that situation constraints should be applied to satisfy the continuity of the material points in the undeformed configuration.

In order to compute the control point displacements $\mathbf{U}_{i,j} \in \mathbb{R}^2$ we rewrite equation (12) as

$$\mathbf{u}(\xi,\eta) = \sum_{i=1}^{n}\sum_{j=1}^{s} R_{i,j}^{p,t}(\xi,\eta)\mathbf{U}_{i,j} = \left[R_{1,1}^{p,t}(\xi,\eta)\mathbf{I}\ldots R_{n,s}^{p,t}(\xi,\eta)\mathbf{I}\right]\begin{pmatrix}\mathbf{U}_{1,1}\\ \vdots \\ \mathbf{U}_{n,s}\end{pmatrix} = \mathbf{R}(\xi,\eta)\mathbf{a} \qquad (13)$$

with $\mathbf{a} \in \mathbb{R}^{2ns}$ being the state vector and $\mathbf{I}$ the 2×2 identity matrix. Similarly, we can express the engineering strain and displacement jump over the discontinuity Γ_d in terms of the state vector as

$$\begin{aligned}\boldsymbol{\gamma}(\xi,\eta) &= \sum_{i=1}^{n}\sum_{j=1}^{s}\mathbf{B}_{i,j}(\xi,\eta)\mathbf{U}_{i,j} = \mathbf{B}(\xi,\eta)\mathbf{a} &(14)\\ [\![\mathbf{u}]\!](\xi,\eta) &= \sum_{i=1}^{n}\sum_{j=1}^{s}\mathbf{M}_{i,j}(\xi,\eta)\mathbf{U}_{i,j} = \mathbf{M}(\xi,\eta)\mathbf{a} &(15)\end{aligned}$$

in which

$$\begin{aligned}\mathbf{B}_{i,j}(\xi,\eta) &= \begin{bmatrix} \frac{\partial R^{p,t}_{i,j}}{\partial\xi}\frac{\partial\xi}{\partial x}+\frac{\partial R^{p,t}_{i,j}}{\partial\eta}\frac{\partial\eta}{\partial x} & 0\\ 0 & \frac{\partial R^{p,t}_{i,j}}{\partial\xi}\frac{\partial\xi}{\partial y}+\frac{\partial R^{p,t}_{i,j}}{\partial\eta}\frac{\partial\eta}{\partial y}\\ \frac{\partial R^{p,t}_{i,j}}{\partial\xi}\frac{\partial\xi}{\partial y}+\frac{\partial R^{p,t}_{i,j}}{\partial\eta}\frac{\partial\eta}{\partial y} & \frac{\partial R^{p,t}_{i,j}}{\partial\xi}\frac{\partial\xi}{\partial x}+\frac{\partial R^{p,t}_{i,j}}{\partial\eta}\frac{\partial\eta}{\partial x}\end{bmatrix} &(16)\\ \mathbf{M}_{i,j}(\xi,\eta) &= \begin{cases}\lim_{\epsilon\to 0}\left(R^{p,t}_{i,j}(\xi_{\mathrm{d}}+\epsilon,\eta)-R^{p,t}_{i,j}(\xi_{\mathrm{d}}-\epsilon,\eta)\right)\mathbf{I} & \xi=\xi_{\mathrm{d}}\\ \lim_{\epsilon\to 0}\left(R^{p,t}_{i,j}(\xi,\eta_{\mathrm{d}}+\epsilon)-R^{p,t}_{i,j}(\xi,\eta_{\mathrm{d}}-\epsilon)\right)\mathbf{I} & \eta=\eta_{\mathrm{d}}\\ \mathbf{0} & \text{otherwise}\end{cases} &(17)\end{aligned}$$

with $\mathbf{0}$ being the 2×2 zero matrix. Computation of the matrix in equation (16) requires the evaluation of the Jacobian, which is computed by evaluation of the partial derivatives of the parameterization (10). Substitution of the equations (13), (14) and (15) in the weak form, equation (3), yields the non-linear system of equations

$$\mathbf{f}_{\mathrm{int}}(\mathbf{a}) = \mathbf{f}_{\mathrm{ext}} \tag{18}$$

with

$$\begin{aligned}\mathbf{f}_{\mathrm{int}}(\mathbf{a}) &= \int_{\Omega}\mathbf{B}^{\mathrm{T}}\boldsymbol{\sigma}\,\mathrm{d}\Omega+\int_{\Gamma_{\mathrm{d}}}\mathbf{M}^{\mathrm{T}}\mathbf{t}([\![\mathbf{u}]\!])\,\mathrm{d}\Gamma_{\mathrm{d}} &(19)\\ \mathbf{f}_{\mathrm{ext}} &= \int_{\Gamma_{\mathrm{d}}}\mathbf{R}^{\mathrm{T}}\hat{\mathbf{t}}\,\mathrm{d}\Gamma_{\mathrm{d}} &(20)\end{aligned}$$

The Dirichlet constraints are satisfied by means of constraints on the state vector $\mathbf{a}$, corresponding to the control point displacements $\mathbf{U}_{i,j}$ with nonzero contributions on Γ_u. A Newton-Raphson solution procedure is then used to solve the non-linear system of equations (18). The integrals (19) and (20) are evaluated in the parameter domain using a Gaussian quadrature, as discussed in Ref. [13]. Improved performance can likely be obtained by considering more advanced integration rules [25].

As a consequence of the definition of a NURBS patch, a discontinuity inevitably propagates throughout a complete patch. In some cases, such as that shown in Figure 4, this allows for the parameterization of a body with a discontinuity. However, for the more general case of Figure 1, the body Ω with discontinuities Γ_{d} cannot be described by a single NURBS patch. One approach to this problem is to use multiple NURBS patches, tied together with C^0 constraints on patch boundaries [13]. In this way, a broad range of bodies with pre-defined discontinuities can be discretized.

3.3. Discretization of a solid with propagating discontinuities using T-splines

Combining NURBS patches is generally a cumbersome task. This is particularly so when a propagating discontinuity is considered, since the partitioning of the computational domain by NURBS patches needs to be performed after each nucleation or propagation. For propagating discontinuities it is therefore attractive to use T-splines.

T-splines were introduced by Sederberg et al. [26] and have recently been used for analysis purposes [27]. Another application of T-splines can be found in [28]. T-splines are a generalization of NURBS in the sense that NURBS are a particular class of T-splines. The motivation behind a T-spline can be understood by first considering the localization of a single basis function in a B-spline or NURBS patch. The basis function $R_{i,j}^{p,t}$ may be completely defined by a set of local knot vectors $\Xi_{i,j} \subset \Xi$ and $\mathcal{H}_{i,j} \subset \mathcal{H}$ of length $p+2$ and $t+2$, respectively. In the case that the orders p and t are odd, to which we will restrict ourselves in this work, the knot vectors associated with the vertex (i,j) in the index space are $\Xi_{i,j} = \left\{\xi_{i-\frac{p+1}{2}}, \dots, \xi_i, \dots, \xi_{i+\frac{p+1}{2}}\right\}$ and $\mathcal{H}_{i,j} = \left\{\eta_{i-\frac{t+1}{2}}, \dots, \eta_i, \dots, \eta_{i+\frac{t+1}{2}}\right\}$ with $i \in \left\{\frac{p+3}{2}, \dots, \frac{2n+p+1}{2}\right\}$ and $j \in \left\{\frac{t+3}{2}, \dots, \frac{2s+t+1}{2}\right\}$. The upper NURBS patch in Figure 4 can therefore also be represented by means of a T-mesh as shown in the top left picture of Figure 5. Note that in the representation of the T-mesh the outer indices are omitted since the basis functions associated with these vertices are zero over the elements (gray areas in Figure 5). If the local knot span of a basis function falls outside the index space, the boundary index is repeated as many times as necessary. To illustrate this, we present the local knot vectors for the upper mesh in Figure 5 in Appendix I. Obviously, the number of T-spline basis functions in this case equals ns, the same as for the NURBS patch in Figure 4.

The T-mesh allows for the insertion of discontinuity boundaries locally. In contrast to the NURBS case discussed in the previous section, a discontinuity can be inserted that does not span the complete width of the index space. If we again consider the example of inserting a crack at $\eta_{\mathrm{d}} = \frac{1}{3}$, we restrict the discontinuity to the leftmost element, by only inserting horizontal knot lines in the index space until $i = 6$ (in the middle pictures of Figure 5). We present the local knot vectors for this T-spline mesh in Appendix I. Note that the local knot vectors of the basis functions in the vicinity of the discontinuity are changed, whereas those away from the crack remain unchanged. The crack can propagate by extending the horizontal knot lines in the index space associated with the discontinuity, as shown in the bottom pictures of Figure 5. As can be seen from Figure 5, we extend the knot line throughout the complete T-spline mesh in the parameter and physical space. It is, however, emphasized that only a part of this knot line represents a line of decreased continuity, as indicated by the bold lines in the physical space. In this work we refer to the shaded areas in the parameter space as elements, which differs from the definition adopted in Ref. [29], where element boundaries are associated with lines of decreased continuity.

In Figure 5 the insertion of a C^{-1} line in the horizontal direction (at $\eta_{\mathrm{d}} = \frac{1}{3}$) is accompanied by the insertion of C^0 lines (with multiplicity equal to the order) in the vertical direction at $\xi = \frac{1}{3}$ in the center pictures, and additionally at $\xi = \frac{2}{3}$ in the bottom pictures. These C^0 lines are introduced to shield the crack segments from the rest of the domain and from each other. This is required to satisfy the condition that a crack can only propagate such that $\Gamma_{\mathrm{d}}(t) \subseteq \Gamma_{\mathrm{d}}(t + \Delta t)$. Moreover, it allows us to parameterize a crack with the minimum number of basis functions, denoted by the $\oplus$ points in Figure 5. Note that additional control points are inserted at $(i,j) \in [5,6] \otimes [3,6]$ in the center picture to shield the crack from e.g. the

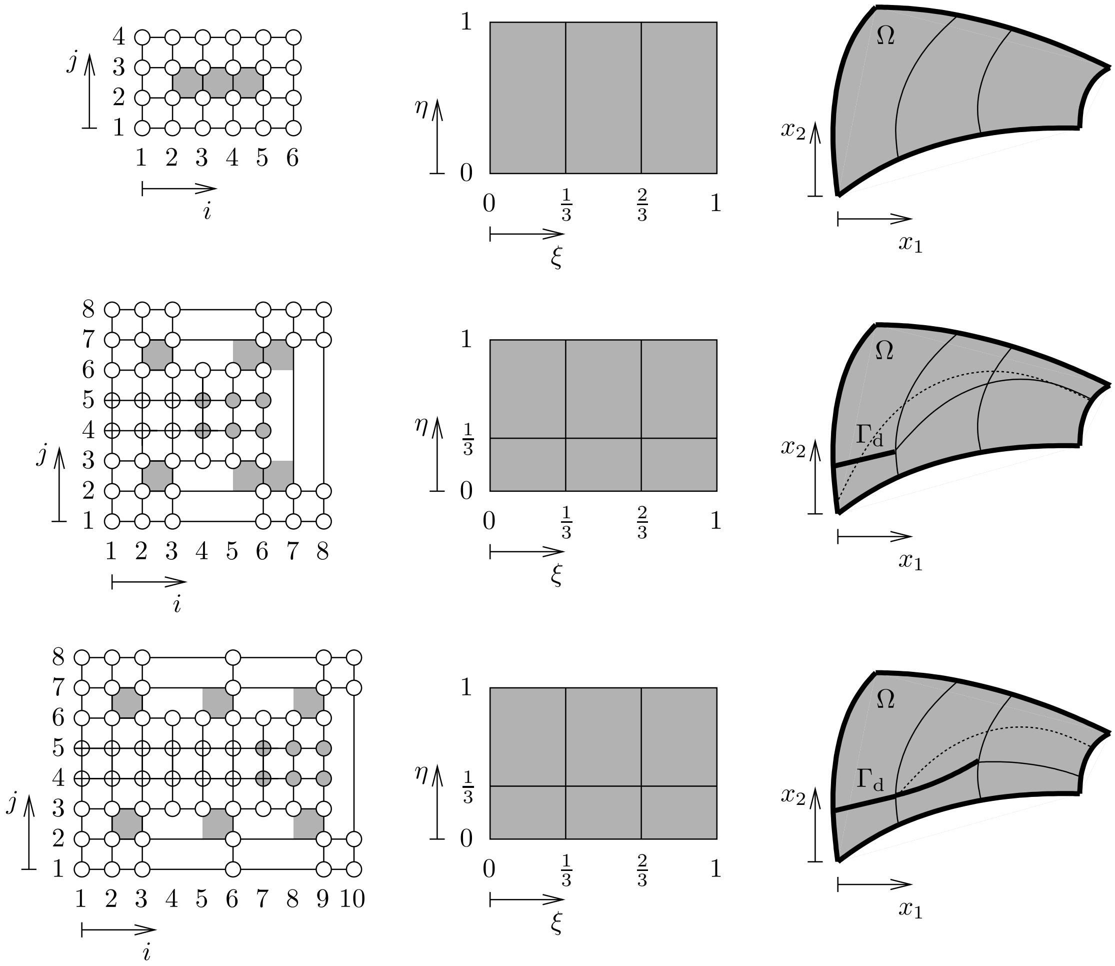

Figure 5. Index space, parameter space and physical space for a T-mesh with a propagating discontinuity Γ_d at $\eta = \eta_d = \frac{1}{3}$. The control points associated with nonzero basis functions at the discontinuity are indicated by $\oplus$. The control points to which constraints are applied to prevent crack opening in front of the crack tip are indicated with a gray background. In the physical space it is observed that the parameterization of the body Ω is changed when a cohesive segment is inserted. To clarify this, the isoparameter, $\eta = \eta_d$, before reparameterization is indicated by the dotted line in the physical space. The local knot vectors for the upper two T-spline meshes are provided in Appendix I.

basis function associated with vertex $(6, 2)$. Unfortunately, insertion of these additional control points allows the discontinuity to also extend in the element in front of the crack tip. This is prevented by constraining these basis functions (control points with gray background) such that the displacement field in front of the crack tip remains continuous. We also constrain the control points associated with the crack tip (the $\oplus$ with gray background) in order to prevent the crack tip from opening, i.e., we require that $[\![\mathbf{u}]\!] = \mathbf{0}$ at the crack tip.

In the case of third-order basis functions the parameterization of a crack requires the provision of four relations in the case that the crack path is parameterized by means of a polynomial (the control point weights are all taken equal). These relations are provided by prescribing the position of the crack at both sides of a segment, as well as its normal vectors. A continuous crack path is then obtained by matching the end point of one segment to the starting point of the next. The differentiability of the crack path is assured by matching the normal vectors of two adjacent crack segments. Some details on the parameterization of the crack path are provided in section 4.2.

Upon the extension of a crack, the parameterization of the body Ω is in general changed. In Figure 5 this is visualized by the isoparametric line for $\eta = \eta_{\mathrm{d}}$. This line moves through the domain Ω when a cohesive segment is inserted. Before reparameterization of the geometry, the isoparametric line corresponding to $\eta = \eta_{\mathrm{d}}$ (dotted lines in the physical space) is not aligned with the discontinuity boundary Γ_{d}. Reparameterization of the geometry shifts the isoparameter in order to align it with the discontinuity boundary. For the cohesive zone formulation this reparameterization is not a fundamental problem, but it requires careful algorithmic consideration, see section 4.3.

Since in the case of a T-mesh the approximation of the displacement field can also be expressed in the form of equation (12), the discretization procedure is exactly the same as for the NURBS discussed in section 3.2. The fact that the number of basis functions changes upon the insertion of a cohesive segment, requires the recomputation of the converged state vector. Redetermination of the history parameters is also required due to the change in parameterization of the body Ω. These algorithmic aspects are discussed in section 4.4.

4. ALGORITHMIC ASPECTS

In this section some algorithmic aspects that are important for the implementation of the isogeometric framework are discussed. These algorithmic aspects are primarily related to the modeling of propagating discontinuities.

4.1. Direction and instance of propagation

As in the case of partition of unity-based finite element models for discrete fracture, a C^0 continuity condition exists at the crack tip. As a result, the stress tensor at the crack tip is generally not uniquely defined. The instance of propagation is determined on the basis of the stress tensor in the integration point closest to the crack tip. If the fracture strength of the material is exceeded, crack propagation is assumed. Crack nucleation is governed by the same criterion, evaluated for the stress tensors in all integration points.

As is done in partition of unity-based models, the direction of nucleation of a crack is based on a smoothed stress tensor as suggested in [30]. The smoothed stress is determined using the

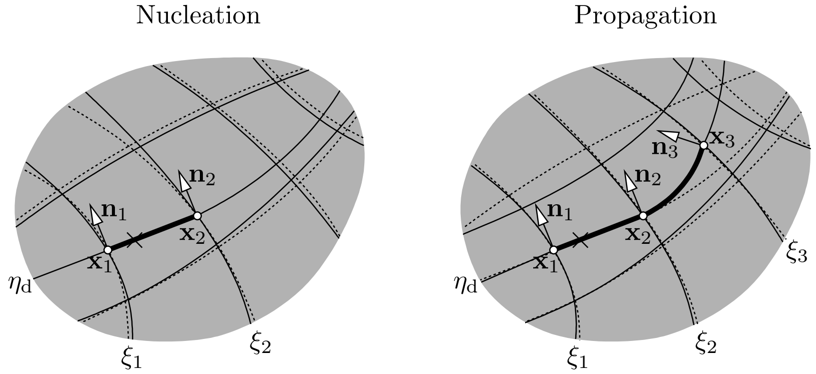

Figure 6. Schematic representation of the crack path after nucleation and propagation. The isoparametric lines before (dotted) and after (solid) reparameterization are shown.

weighting function used in [9]

$$w = \frac{1}{(2\pi)^{\frac{3}{2}} l^3} \exp\left(-\frac{\|\mathbf{x} - \mathbf{x}_{\text{tip}}\|^2}{2l^2} \right) \tag{21}$$

In this weighting function, which should not be confused with the NURBS weighting function introduced in section 3.1, l is the smoothing length and $\mathbf{x}_{\text{tip}}$ is the position of the crack tip. Use of this smoothed stress measure for the determination of the normal vector was found to improve the reliability of the observed crack path, especially on coarse meshes.

4.2. Crack path parameterization

As discussed in section 3.3, in the isogeometric approach a crack is extended per element. In the case that an isoparametric description of order three or higher is considered, a crack path can be created with a continuous normal vector, as illustrated in Figure 6. The maximum attainable smoothness of the crack path increases with increasing order of the isogeometric discretization. In this work, we restrict ourselves to continuously differentiable cracks. However, we emphasize that smoother crack parameterizations can be derived for isogeometric discretizations with orders higher than these considered in this contribution. If the stress criterion is violated in an integration point (indicated by × in Figure 6), a straight cohesive segment is inserted through that integration point with the normal vector corresponding to the direction of the maximum principal stress. Based on the direction of the normal vector, the crack is modeled either as a horizontal or as a vertical crack in the index and parameter space. Note that in Figure 6 the crack runs horizontally through the parameter domain. The crack tips $\mathbf{x}_1$ and $\mathbf{x}_2$ are determined as the intersections of the straight cohesive segment with the isoparameteric lines corresponding to the element boundaries before reparameterization.

When a tip violation is encountered, the crack is extended over one element, as shown in Figure 6. The starting point of the inserted curved crack segment is described by the position and normal vector of the violated tip ($\mathbf{x}_2$ and $\mathbf{n}_2$). The normal vector at the end point $\mathbf{n}_3$ is required to match the principal direction of the stress tensor. The end position of the new segment $\mathbf{x}_3$ is determined as the intersection of the crack path with the isoparametric line corresponding to ξ_3 before reparameterization. To compute this intersection, it is assumed that the normal and corresponding tangent vary linearly from $\mathbf{n}_2$ at ξ_2 to $\mathbf{n}_3$ at ξ_3. After the insertion of a cohesive segment, the parameterization of the interior of the domain is altered, as indicated by the difference between the solid and dotted lines in Figure 6. The required reparameterization of the domain is discussed next.

4.3. Determination of the T-mesh control net

In computer aided design, NURBS and T-splines (among others) are used to parameterize the geometry. When changes are made to the topology of the mesh, it is desirable to preserve the parameterization. As mentioned in section 3.2, for NURBS, efficient refinement algorithms exist which preserve parameterization. A T-spline refinement algorithm which preserves parameterization was proposed in [31], but appeared to be non-local when applied in an adaptive analysis environment. The development of efficient local refinement strategies for analysis suitable T-splines is an area of active research [32].

The fact that efficient and robust algorithms for T-spline refinement are not yet generally available, however, does not prohibit the type of analysis considered here. This is because the requirements on the preservation of the parameterization when changing the T-mesh topology are less strict in cohesive zone analyses than in design, where the geometry must be preserved exactly. Of course, it is of crucial importance that the boundaries of the physical domain, including the cracks, remain in the same position. However, the parameterization of the interior of the domain does not necessarily need to be conserved, as long as the mesh quality remains satisfactory. In practice this means that the curvatures of the elements should remain bounded. In this respect, the isogeometric approach is not much different from classical finite elements, in which the exact position of the elements is often of minor importance as long as the mesh quality is acceptable.

In this contribution we determine the inner control point positions for each T-mesh by requiring the geometry to minimize the gradients in the parameterization in some sense. We solve different problems to determine an initial mesh and for the control net evolution after the insertion of a cohesive segment. For notational convenience we use index notation in this subsection. The physical and parametric position vectors are given by $x \in \mathbb{R}^2$ and $\xi \in \mathbb{R}^2$, respectively.

- In order to determine the control net for an initial mesh, and its mesh refinements, we solve an elliptic problem on the parameter domain (here denoted by Ω^ξ). The problem considered here is inspired by the elasticity problem, which minimizes the gradients in the displacement field. Here we consider a simple problem that is anticipated to minimize the gradients in the geometry parameterization. The problem is given by

$$\begin{cases} \frac{\partial}{\partial \xi_j}\left(\delta_{ij}\psi_{kk} + \psi_{ij}\right) = 0 & \xi \in \Omega^\xi \\ x_1 = \hat{x}_1 & \xi \in \Gamma^\xi_{x_1} \\ x_2 = \hat{x}_2 & \xi \in \Gamma^\xi_{x_2} \\ x = \hat{x}_\mathrm{d} & \xi \in \Gamma^\xi_\mathrm{d} \end{cases} \tag{22}$$

  while minimizing the variation in the control weights. In these equations, $\psi_{ij} = \frac{1}{2}\left(\frac{\partial x_i}{\partial \xi_j} + \frac{\partial x_j}{\partial \xi_i}\right)$ and $\Gamma^\xi_{x_1}$ and $\Gamma^\xi_{x_2}$ are the boundaries of the parameter domain on which the position components $\hat{x}_1$ and $\hat{x}_2$ are prescribed. The crack position is described by $\hat{x}_{\mathrm{d}}$ on the internal boundary $\Gamma_{\mathrm{d}}^{\xi}$. Solving the system of equations (22) minimizes the derivatives of the the physical position vector with respect to the parametric position vector and therefore prevents the occurrence of steep gradients in the geometry parameterization. To illustrate this, we again consider the uniform one-dimensional rod introduced in section 3.1. In that case the problem (22) reduces to $\frac{\mathrm{d}^2 x}{\mathrm{d}\xi_2} = 0$ with boundary conditions $x(0) = 0$ and $x(1) = L$, which results in the linear parameterization $x = L\xi$.

- The update of the control net after the insertion of a cohesive segment is determined by computing the displacement v of the physical positions with respect to the original parameterization x. Here we determine the displacement field v by solving a problem on the physical domain Ω, given by

$$\begin{cases} \frac{\partial^2 v_1}{\partial x_1^2} = 0 & x \in \Omega \\ \frac{\partial^2 v_2}{\partial x_2^2} = 0 & x \in \Omega \\ v_1 = 0 & x \in \Gamma_{v_1} \\ v_2 = 0 & x \in \Gamma_{v_2} \\ v = \hat{v} & x \in \Gamma_{\mathrm{d}} \end{cases} \tag{23}$$

such that the new positions of the physical space are given by $\tilde{x} = x + v$. The change in position required to model the crack, $\hat{v}$, is provided by the crack path as described in section 4.2. As for the initial meshes, this system of equations is solved while minimizing the variation in the control weights. The problem (23) minimizes the gradient of the parameterization in a different way than problem (22). For the numerical simulations considered in section 5, updating the parameterization using problem (23) was found to yield more robust results than using problem (22). In the case of the composite rod introduced in section 3.1, the update scheme (23) reduces to $\frac{\mathrm{d}^2 v}{\mathrm{d}x^2} = 0$ with boundary conditions $v(0) = v(L) = 0$ and $v(\frac{1}{3}L) = \hat{v} = 0$, which results in $v = 0$ and hence preserves the parameterization.

The formulations that we used for both cases have proven their suitability for the numerical simulations considered in section 5, but we emphasize that they are by no means optimal. Improvement of the control net update schemes is a topic of further study.

4.4. State-vector and history values update

As discussed in section 2, a staggered solution scheme is used to trace the evolution of a crack path. This means that if at some point in the simulation an equilibrium solution $\mathbf{u}(\mathbf{x}) = \mathbf{R}(\mathbf{x})\mathbf{a}$ is found in the form of the state vector $\mathbf{a}$, it is possible that this equilibrium state triggers a crack extension and as a consequence results in a change in the T-mesh topology. As a result, the equilibrium state vector $\mathbf{a}$ is no longer the discrete form of the equilibrium solution $\mathbf{u}(\mathbf{x})$. In fact, the updated T-mesh will consist of more basis functions than the T-mesh on which $\mathbf{a}$ was determined. Since the next equilibrium state is determined as an increment to the previously converged state vector, it is necessary to determine the state vector $\tilde{\mathbf{a}}$ corresponding to the equilibrium solution $\mathbf{u}(\mathbf{x})$ on the updated mesh. We achieve this by minimizing

$$\mathcal{E} = \int_{\Omega} \left\| \tilde{\mathbf{R}}(\mathbf{x})\tilde{\mathbf{a}} - \mathbf{u}(\mathbf{x}) \right\|^2 \mathrm{d}\Omega \tag{24}$$

with $\tilde{\mathbf{R}}$ being the T-mesh basis functions on the updated mesh. The updated state vector can then be determined by solving a linear problem. In the case that the solution space of the old T-mesh is nested in the new mesh, the functional $\mathcal{E}$ in equation (24) will minimize to zero.

Since the parameterization of the body Ω changes upon the insertion of a cohesive segment, it can also be required to update the history parameters in the integration points. This situation is not encountered here, since history parameters are only considered for the integration points on the discontinuity boundary, for which the parameterization does not change. In the situation that history parameters are also used for the interior integration points, their updated values can be determined by solving a minimization problem similar to that in equation (24).

5. NUMERICAL SIMULATIONS

We illustrate the isogeometric discretization methods using various typical cohesive zone simulations. First, we demonstrate the use of a NURBS-based discretization for modeling the debonding process between a circular fibre and the epoxy it is embedded in. In this example the fracture surface is fixed throughout the debonding process, allowing for the use of NURBS and NURBS surfaces. In the second and third numerical simulations we consider propagating cracks, requiring the use of T-spline discretizations. The second simulation demonstrates the interaction between an adhesive and a cohesive crack, whereas in the third numerical experiment multiple cracks appear, including a strongly curved crack. Mesh convergence studies are presented for all numerical simulations. In those studies it is important to note that the scaling of the number of degrees of freedom with the number of elements differs from that in the case of traditional finite elements.

5.1. Fibre-epoxy debonding experiment

We consider a fibre with a 5 μm radius embedded in a $30 \times 30\,\mu m$ square block of epoxy (Figure 7), as introduced in [33]. The depth of the specimen is assumed to be much larger than the other dimensions, hence a plane strain assumption is adopted. The specimen is loaded in the horizontal direction by gradually increasing the displacement $\bar{u}$ of the left and right edges. Contraction of the epoxy specimen in the vertical direction is prohibited by roller supports on the upper and lower edges of the block. The symmetry of the specimen allows to restrict the computational domain to the top right quadrant of the specimen, in combination with horizontal rollers along the x_1-axis and vertical rollers along the x_2-axis.

A linear elastic isotropic material description is used for both the fibre and the epoxy. For the epoxy a modulus of elasticity, i.e. the Young's modulus, of 4.3 GPa and Poisson's ratio of 0.34 is used. The fibre is much stiffer with a modulus of elasticity of 225.0 GPa and a Poisson's ratio of 0.2. The traction on the fibre-epoxy interface is related to its opening by means of the Xu-Needleman law [34]. The fracture strength and fracture toughness in normal (mode I) and shear (mode II) are taken equal to $t_{\mathrm{ult}} = 50\,\mathrm{MPa}$ and $\mathcal{G}_{\mathrm{c}} = 4 \cdot 10^{-3}\,\mathrm{N/mm}$, respectively. Assuming the opening in the normal direction after complete shear failure to be equal to zero

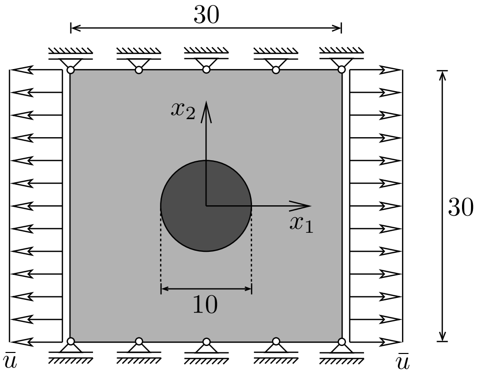

Figure 7. Schematic representation of a fibre with a circular cross section embedded in a square block of epoxy. All dimensions are in micrometers.

in the case of zero normal traction, the traction-opening relations are given by

$$t_n = \frac{\mathcal{G}_c}{\delta_n}\frac{[\![u_n]\!]}{\delta_n}\exp\left(-\frac{[\![u_n]\!]}{\delta_n}\right)\exp\left(-\frac{[\![u_s]\!]^2}{\delta_s^2}\right) \tag{25}$$

$$t_s = \frac{2\mathcal{G}_c}{\delta_s}\frac{[\![u_s]\!]}{\delta_s}\left(1+\frac{[\![u_n]\!]}{\delta_n}\right)\exp\left(-\frac{[\![u_n]\!]}{\delta_n}\right)\exp\left(-\frac{[\![u_s]\!]^2}{\delta_s^2}\right) \tag{26}$$

in the case of loading. The parameters δ_n and δ_s are the characteristic length parameters that are related to the fracture strength and fracture toughness by $\delta_n = \mathcal{G}_c/(t_{\text{ult}}e)$ and $\delta_s = \mathcal{G}_c/(t_{\text{ult}}\sqrt{\frac{1}{2}e})$ with $e = \exp(1)$. The loading condition is checked on the basis of the history parameter κ and the loading function $f = \sqrt{\langle[\![u_n]\!]\rangle^2 + \beta^{-1}[\![u_s]\!]^2} - \kappa$, with $\langle[\![u_n]\!]\rangle = \frac{1}{2}\left(|[\![u_n]\!]| + [\![u_n]\!]\right)$ and $\beta = 2.3$ the mode-mixity parameter. The history function f evolves according to the Kuhn-Tucker conditions

$$f \leq 0 \qquad \dot{\kappa} \geq 0 \qquad \dot{\kappa}f = 0 \tag{27}$$

In the case of unloading ($f < 0$), the traction components are related to the crack opening by means of the secant stiffnesses. Finally an additional penetration stiffness $k_{\text{p}} = 1\cdot 10^5$ MPa/mm is added in the normal direction in the case of negative crack opening in the normal direction.

The response of the fibre-epoxy system is determined using four different quadratic ($p = t = 2$) NURBS meshes. The coarsest mesh, consisting of only 8 elements (64 DOFs), is shown in Figure 8. As can be seen, an attractive feature of the used discretization is that the geometry is represented exactly with only 8 elements. In order to create the discontinuity in the radial direction, the knot that coincides with the interface is given a multiplicity of $p + 1 = 3$. In Figure 8 two subsequent uniform mesh refinements are also shown, with 32 elements (144 DOFs) and 128 elements (400 DOFs), respectively. In addition, the response of the system was determined using a mesh with 2048 elements (4644 DOFs), which we refer to as the reference solution.

The response of the system is measured in terms of the $\sigma_{x_1x_1}$ stress at $\mathbf{x} = (15, 0)\,\mu$m versus the prescribed displacement of the left and right edges. Initially displacement control

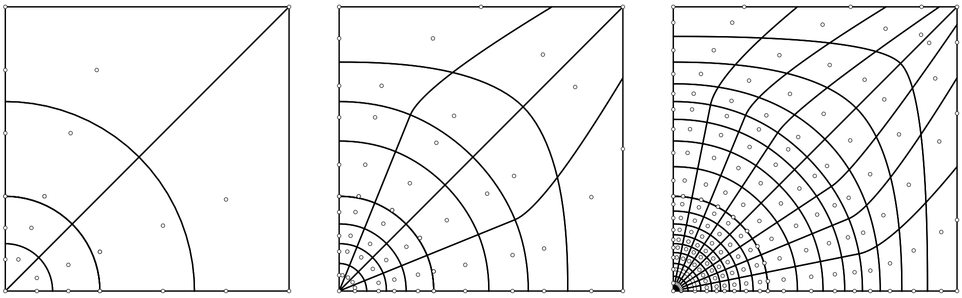

Figure 8. NURBS meshes used for the fibre-epoxy simulations. Note that typically the control nodes do not coincide with the element vertices.

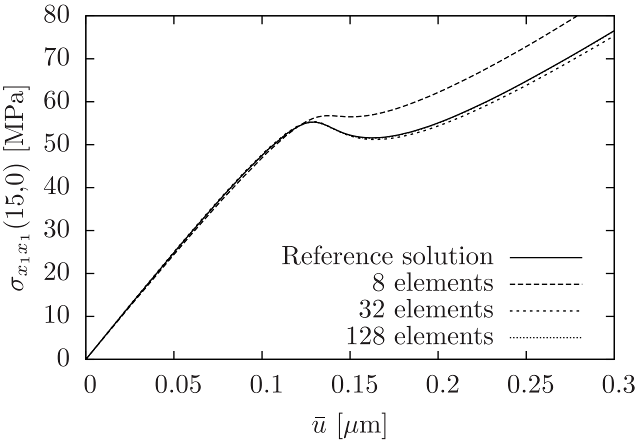

Figure 9. Response curves for the fibre-epoxy system determined using various meshes. The stress component $\sigma_{x_1x_1}$ at $\mathbf{x} = (15, 0)$ μm is plotted versus the horizontal displacement $\bar{u}$. Note that the response using 128 elements coincides with that of the reference solution (2048 elements).

is used in which $\bar{u}$ increases with steps of $2.5 \cdot 10^{-2}\,\mu$m. Once $1 \cdot 10^{-8}$ mJ (per unit depth of the specimen) of energy is dissipated in a step, energy release rate control [35] is used with steps of $5 \cdot 10^{-7}$ mJ. The response curves for the various NURBS meshes are shown in Figure 9. The reference solution is in excellent agreement with the results reported in [33], which were obtain using a partition of unity-based finite element discretization with 2500 linear quadrilateral elements. The result determined using 128 elements coincides with that of the reference solution and is therefore not visible in Figure 9. As can be seen, the curve obtained using 32 elements is already in good agreement with the reference solution. With only 132 degrees of freedom (66 control points for the 32 elements mesh), the performance of the NURBS discretization compares favorably with those obtained using the partition of unity method in terms of computational effort [33] .

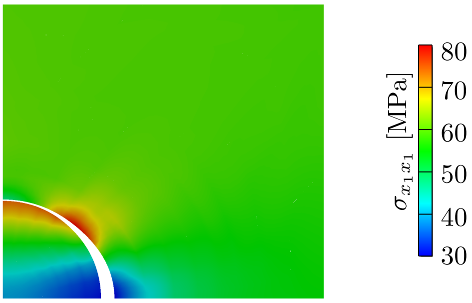

Figure 10. Contour plot showing the $\sigma_{x_1x_1}$ stress in the fibre-epoxy system at $\bar{u} = 0.165\,\mu$m using the 128 elements discretization. Displacements are amplified by a factor of 10.

From the response curves it is observed that initially the stress in the measurement point increases as the edge displacement increases. As the ultimate load is reached, the fibre and epoxy start to debond, leading to a softening regime in the response curve. After the fibre and epoxy have fully debonded, the force again increases as the epoxy remains carrying the loads. The debonding process is visualized in the contour plot shown in Figure 10. From this contour plot it is also observed that the $\sigma_{x_1x_1}$ component (as well as the other components) of the stress is continuous in either of the two subdomains. This is a consequence of the C^1 continuous fields that are obtained using second-order NURBS. In addition, we see that the multiplicity of three of the knot representing the interface indeed results in a discontinuity in the displacement field.

5.2. *Double cantilever beam experiment*

The second numerical experiment we consider is the double cantilever beam as introduced in [36]. The two cantilever beams shown in Figure 11 are connected by an adhesive layer and are loaded by a force P at the bottom right tip of the lower beam. The beams are assumed to have unit depth and plane stress conditions are assumed. A small initial notch, with dimensions 1×1 mm, is created in the middle of the upper edge of the upper beam to ensure crack nucleation at that point. Moreover, crack nucleation near the supports is prevented, so that only a crack starting from the notch is obtained. In order to reproduce the simulation in Ref. [36], the crack is forced to nucleate from the center of the notch.

A linear elastic isotropic material law is used for the beams with modulus of elasticity 20 GPa and Poisson's ratio 0.2. We describe the fracture process in the bulk material by means of the cohesive law, e.g. [9]

$$t_n = t_{\text{ult}} \exp\left(-\tfrac{t_{\text{ult}}}{\mathcal{G}_c}\kappa\right) \qquad (28)$$

$$t_s = d_{\text{int}} \exp\left(h_s\kappa\right)[\![u_s]\!] \qquad (29)$$

Here we consider the mode I case, i.e. with $d_{\text{int}} = 0$. For the fracture strength and fracture toughness we take $t_{\text{ult}} = 2.5$ MPa and $\mathcal{G}_c = 0.04$ N/mm, respectively. The history parameter κ is determined by the loading function $f = [\![u_n]\!] - \kappa$, which evolves according to the Kuhn-Tucker conditions (27). In the case of unloading ($f < 0$), the traction components are linearly

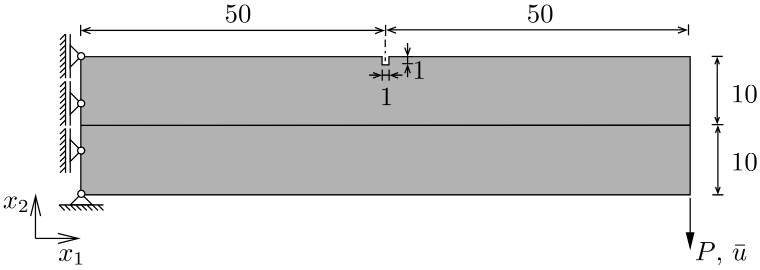

Figure 11. Schematic representation of the double cantilever beam experiment. All dimensions are given in millimeters.

related to those of the opening by their respective secant stiffnesses. In the case of negative normal opening, an additional penetration stiffness of $1 \cdot 10^6$ MPa/mm is added in the normal direction. The tip stress smoothing length in equation (21) is taken equal to 1.8 mm.

The traction-opening behavior of the adhesive layer is governed by the Xu-Needleman law in equation (25) and (26). The fracture strength and fracture toughness are taken as 1.0 MPa and 0.01 N/mm, respectively. The mode-mixity parameter β again equals 2.3 and the penetration stiffness is equal to $k_\mathrm{p} = 100$ MPa/mm.

The geometry and deformation of the double cantilever beam are described using a T-spline mesh. We consider the T-mesh in its index space (Figure 12) and note that the horizontal direction (or i-direction) in the index space coincides with the x_1-direction in the physical space (and the j-direction with the x_2-direction). We restrict ourselves to the use of third-order T-splines ($p = t = 3$). As can be seen in Figure 12, the adhesive interface between the two beams is modeled by creating a knot multiplicity of $t+1 = 4$ in the vertical direction, hence $\eta_4 = \eta_5 = \eta_6 = \eta_7$, which could also be observed from the fact that no elements (shaded area in the plot) are present between the corresponding index lines. Note that this discontinuity runs throughout the complete domain in the horizontal direction, and could also have been described using a single NURBS patch. This is not the case when we consider the representation of the notch in the upper beam. Obviously, in order to create the 90 degree corners in the upper boundary, we require the parameterization to be locally C^0 continuous. This local continuity condition is enforced by inserting additional knots with multiplicity $m = 3$ such that $p - m = 0$. These four groups of three knots (i.e. $\xi_4 = \xi_5 = \xi_6$, $\xi_7 = \xi_8 = \xi_9$, $\xi_{11} = \xi_{12} = \xi_{13}$, $\xi_{14} = \xi_{15} = \xi_{16}$) represent the four corners of the notch. Note that in the case of a NURBS mesh, these inserted C^0 continuities would inevitably propagate throughout a complete patch. In the case of a T-mesh, however, the C^0 continuities can be restricted to where they are needed, i.e. on the upper edge. This is achieved by only inserting additional control points on the upper edge, Figure 12. To illustrate this we consider the knot span in the horizontal direction of the control point (10,10), which changed from $\Xi_{10,10} = \{\xi_2, \xi_3, \xi_{10}, \xi_{17}, \xi_{18}\}$ before the control point insertion to $\Xi_{10,10} = \{\xi_8, \xi_9, \xi_{10}, \xi_{11}, \xi_{12}\}$ after. Hence, on the upper edge the basis functions change. However, if we consider control point (10,8) we observe that the horizontal knot span before and after control point insertion is $\Xi_{10,8} = \{\xi_2, \xi_3, \xi_{10}, \xi_{17}, \xi_{18}\}$, and hence the corresponding basis function is unaffected.

The physical mesh corresponding to the index space of Figure 12 is shown in Figure 13

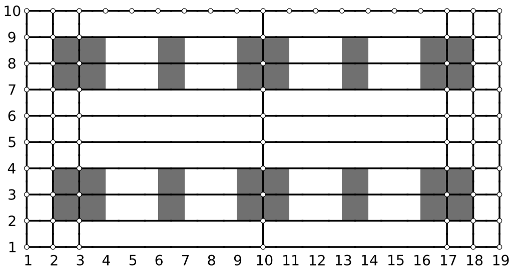

Figure 12. T-mesh in index space used for the representation of the double cantilever beam.

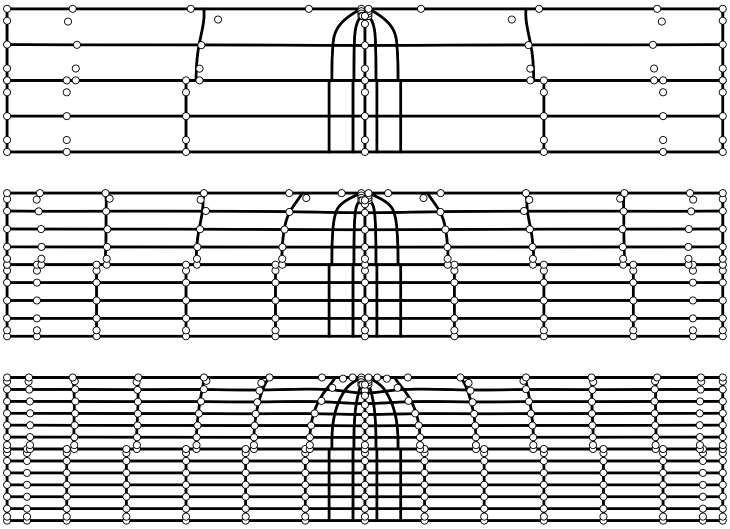

Figure 13. Meshes used for the double cantilever beam simulations. Note that generally the control points do not coincide with the element vertices.

(top), along with two uniform mesh refinements. The coarsest mesh consists of 32 elements, the intermediate mesh of 96 elements, and the finest mesh of 192 elements. Note that in the case of a mesh of T-splines the number of degrees of freedom does not necessarily increase by the same order as the number of elements. The meshes considered here consist of 164, 332 and 564 degrees of freedom, respectively. In Figure 14 we illustrate how the T-spline mesh evolves as the crack propagates. The top figure shows the intermediate T-spline mesh before crack nucleation. In the middle figure, a crack has nucleated from the initial notch and the discontinuity has extended into the first element from the top. The bottom figure shows the T-spline mesh when the crack has propagated though the complete upper beam and is arrested at the adhesive interface.

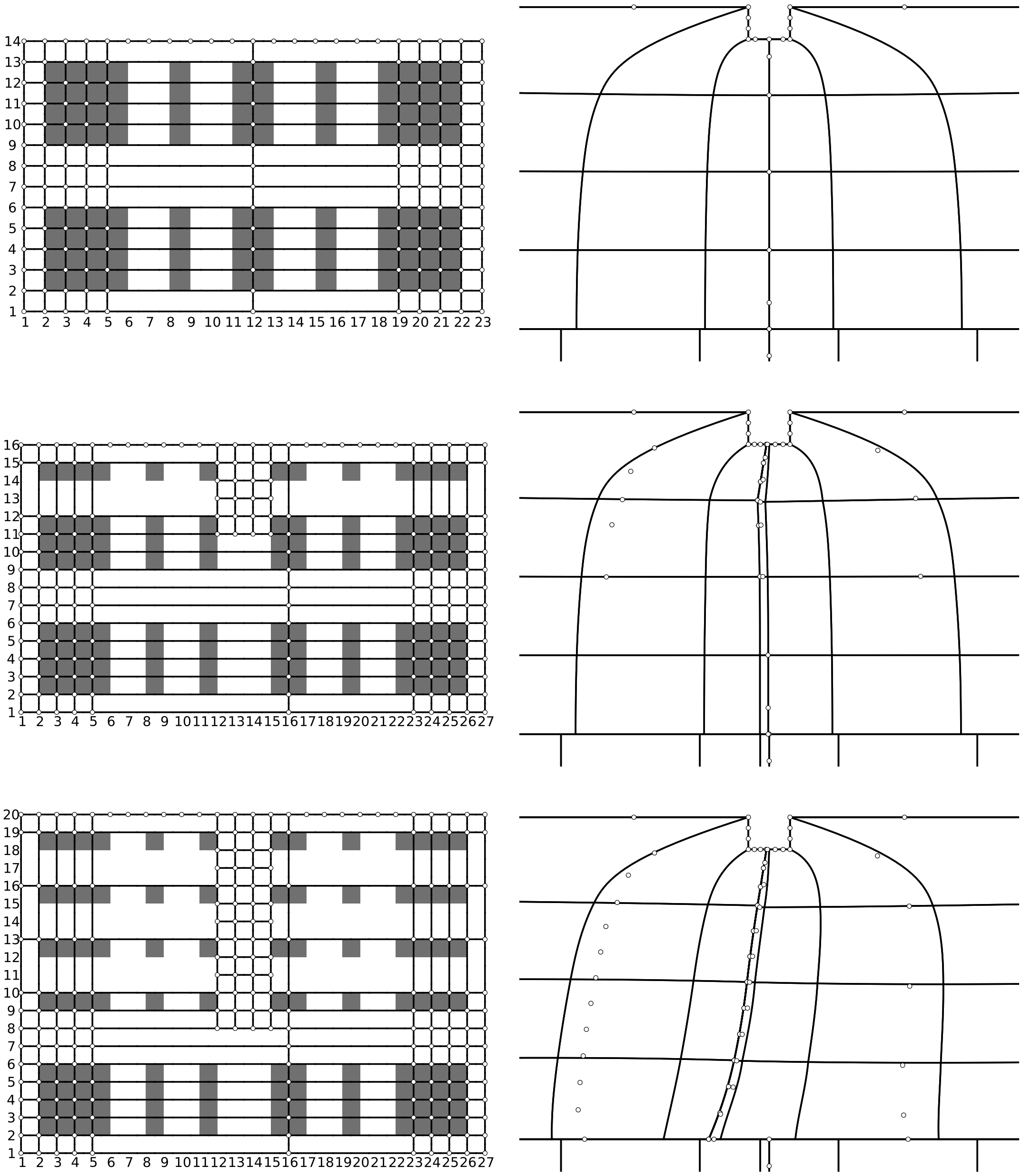

Figure 14. Evolution of the intermediate T-spline mesh as the crack propagates (from top to bottom). The left column shows the mesh in index space, the right column shows the physical mesh in the upper beam around the initial notch.

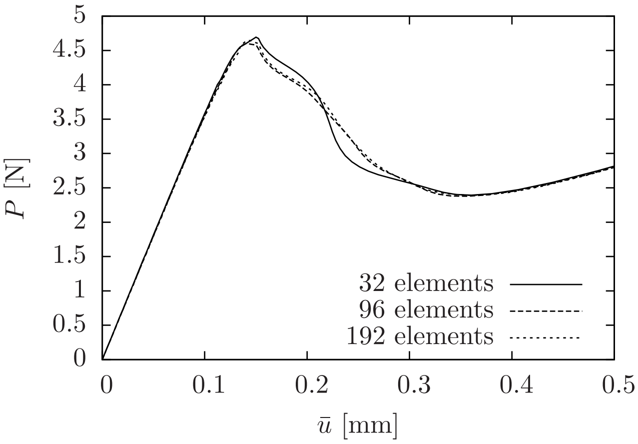

Figure 15. Response of the double cantilever beam measured in terms of the downward force P applied to the right bottom tip of the lower cantilever versus the downward displacement $\bar{u}$ of that point.

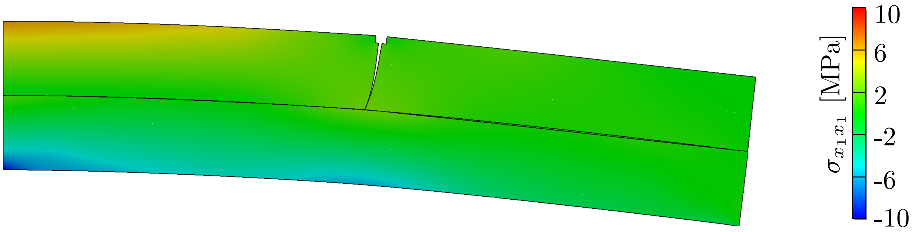

Figure 16. Contour plot showing the $\sigma_{x_1x_1}$ stress in the cantilever beams at $\bar{u} = 0.15$ mm using the finest discretization. Displacements are amplified by a factor of 50.

The response of the double cantilever beam is shown in Figure 15. Initially, the force-displacement curve is traced using displacement control with steps of $2.5 \cdot 10^{-3}$ mm for $\bar{u}$. When 0.01 mJ of energy is dissipated in a single displacement step, energy release control is used with a maximum dissipation step of 0.02 mJ. As can be seen, the response for the intermediate mesh practically coincides with that of the fine mesh, indicating that an accurate solution is obtained using the intermediate mesh. The results are in excellent agreement with these found in [36] where 2079 linear quadrilateral elements were used. As can be observed from the contour plot in Figure 16, a crack nucleates at the notch upon loading and runs downward into the adhesive layer. In contrast to the results reported in [36], the crack is allowed to curve. The effect of this curvature on the global response of the beam is negligible.

5.3. Single-edge notched beam experiment

The third simulation is that of the single-edge notched (SEN) beam, shown in Figure 17. The anti-symmetric loading conditions applied to the specimen create a curved crack that nucleates from the initial notch in the upper edge. Experimental studies of the fracture process

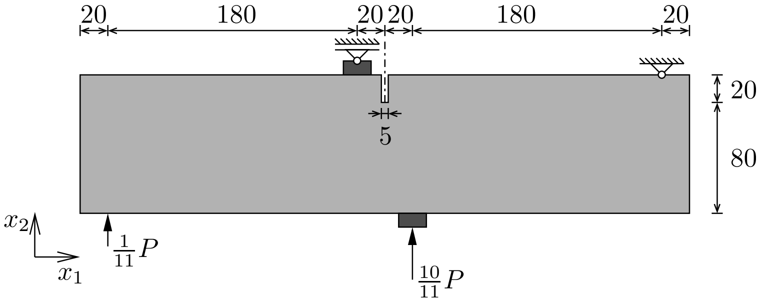

Figure 17. Schematic representation of the single-edge notched (SEN) beam. All dimensions are in millimeters, and the depth of the beam is 100 mm.

in such concrete beams have been performed by Schlangen [37]. Following the first successful numerical simulation of this problem [38], several numerical techniques have been used, such as the partition of unity method [9] and gradient-enhanced continuum damage [39].

The concrete is modeled as a linear elastic isotropic material with modulus of elasticity of 35 GPa and Poisson's ratio 0.15, and plane strain conditions are assumed. As reported in [40] the difference in global response between the plane stress and plane strain case is negligible due to the small Poisson's ratio. The steel loading plates are also modeled with a linear elastic isotropic material law, with a modulus of elasticity of 210 GPa and a Poisson's ratio of 0.3. The fracture process in the concrete is described by the cohesive law introduced in section 5.2. The fracture strength and fracture toughness are taken equal to $t_{\text{ult}} = 2.8\,\text{MPa}$ and $\mathcal{G}_{\text{c}} = 0.1\,\text{N/mm}$, respectively. The initial shear stiffness d_{int} is taken equal to 1 MPa/mm and h_s, which governs the degradation of the shear stiffness, is assumed to be zero. The penetration stiffness is taken as $1 \cdot 10^5$ MPa/mm and the smoothing length in equation (21) has been taken equal to 3.5 mm.

The SEN-beam geometry and the deformation are described using a cubic ($p = t = 3$) T-spline mesh. As can be seen in Figure 18, the T-spline mesh allows for local control point insertion to represent the loading plates and the initial notch. The coarsest mesh which we have considered consists of 130 elements (402 DOFs). Two uniform mesh refinements have been performed, with 334 elements (868 DOFs) and 1204 elements (2734 DOFs), respectively. The equilibrium path is traced using the crack mouth sliding displacement (CMSD), which is defined as the difference in vertical displacement between the notch tips, as the path parameter [38]. The CMSD is increased with steps of $1 \cdot 10^{-3}$ mm. For the coarsest mesh, using the local stress to determine the nucleation direction turned out to yield unrealistic results. For this reason the direction of nucleation was based on the non-local stress as used for the tip stress, with a non-local length of 7 mm. Although not necessary, for consistency this has also been done for the intermediate and the fine mesh.

The response of the SEN-beam computed using the three meshes is shown in Figure 19. The response is measured in terms of the exerted force P versus the CMSD. From Figure 19 it is observed that the result using the intermediate mesh practically coincides with that of the fine mesh. It is therefore concluded that an accurate solution can already be obtained with only 334 elements. From the response it is also observed that the coarsest mesh experiences significant kinks in the response curve (see Figure 19). These kinks in the response curve are caused by

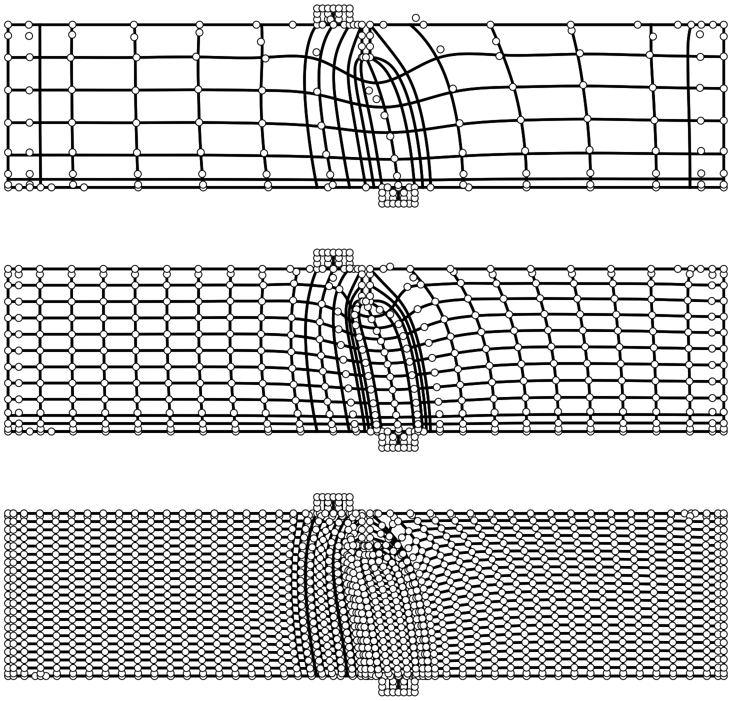

Figure 18. Meshes used for the SEN-beam simulations. Note that the control points do not need to coincide with the element vertices.

the fact that the crack is abruptly extended when the propagation criterion is violated. The more gradual extension of the crack on the finer meshes reduces these effects significantly.

In Figure 20 a contour plot of the cracked SEN-beam is shown. The dominant crack nucleated at the bottom right corner of the initial notch at an angle of 37 degrees with the x_2-axis. As the crack extends it gradually turns to an angle of zero degrees with the vertical axis, which is in good agreement with experimental observations. From the contour plot it can also be observed that a secondary crack nucleates at the bottom edge of the specimen. Also this secondary crack has been observed experimentally. Note from the contour plot that both crack paths are C^1 continuous since the directions of the normal vectors from one segment to another have been matched.

6. CONCLUSIONS

The possibility of enhancing a B-spline basis with discontinuities through knot insertion makes isogeometric finite elements suitable for the capturing of discontinuities, in particular cracks. Non-uniform rational B-splines (NURBS) are useful for problems with pre-defined discontinuities. T-splines are more useful for propagating cracks, since they offer the possibility

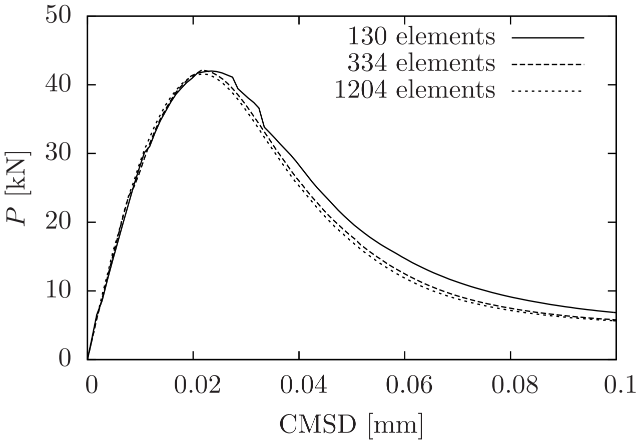

Figure 19. Response curves for the SEN-beam simulations. The response is measured in terms of the applied force P versus the crack mouth sliding displacement (CMSD), which equals the vertical displacement difference between the left and right nodge edges.

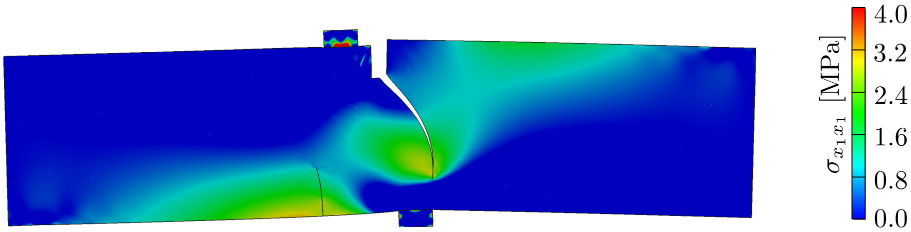

Figure 20. Contour plot showing the $\sigma_{x_1x_1}$ Cauchy stress in the SEN-beam at CMSD=0.033 mm using the finest discretization. Displacements are amplified by a factor of 100.

to create localized discontinuities. From an implementation point of view, the concept of Bézier extraction [29] allows for a unified approach to NURBS and T-splines, and will allow this approach to be extended to T-splines of arbitrary topology.

The capability of NURBS and T-splines to exactly represent a broad range of geometric entities, makes them an attractive alternative for classical finite elements for many problems of engineering interest. Isogeometric finite elements were, for example, found to give an efficient and robust discretization of a fibre-epoxy system. For such problems, an additional advantage of isogeometric analysis is that the geometry obtained from computer aided design can directly be used as a mesh, thereby practically eliminating the analysis costs associated with mesh generation.

For the numerical simulations considered in this work, the isogeometric approach was found to give efficient discretizations in terms of the number of degrees of freedom and the required computational effort. We attribute this efficiency to the higher-order continuity of the basis. The ability to capture smooth stress fields and smooth cracks results in accurate results for relatively coarse meshes. The advantages of higher-order continuity are expected to be more profound in the case of slender structures, making isogeometric finite elements suitable for modeling cracks in, for instance, shells.

The isogeometric approach to cohesive zone formulations is anticipated to be applicable to a broad range of problems with propagating discontinuity boundaries. The configurational force models for brittle fracture [18] are examples of such problems. In this contribution we have enhanced the solution space with discontinuities by means of knot insertion, but isogeometric analysis can also be used in combination with the partition of unity method.

ACKNOWLEDGEMENTS

T. J. R. Hughes and M. A. Scott were partially supported by ONR Contract N00014-08-0992, T. J. R. Hughes was also partially supported by NSF Grant 0700204, and M. A. Scott was also partially supported by an ICES CAM Graduate Fellowship.

APPENDIX

I. T-spline knot vectors: An illustration

To illustrate the definition of the T-spline knot vectors introduced in section 3.3, we present the local knot vectors for the upper two T-spline meshes shown in Figure 5 in Table I and Table II. From Table I it can be seen that if the local knot span of a T-spline basis function falls outside the T-mesh, the boundary knot is repeated. In $\Xi_{2,4}$, for example, knot ξ_1 is duplicated to construct the local knot vector. From Table II it is observed that inserting the discontinuity in the middle mesh of Figure 5 affects some knot vectors, e.g. $\mathcal{H}_{2,3}$, whereas other are unaltered, e.g. $\mathcal{H}_{8,2}$.

i,j	$\Xi_{i,j}$	$\mathcal{H}_{i,j}$	i,j	$\Xi_{i,j}$	$\mathcal{H}_{i,j}$
1,1	$\{\xi_1,\xi_1,\xi_1,\xi_2,\xi_3\}$	$\{\eta_1,\eta_1,\eta_1,\eta_2,\eta_3\}$	1,3	$\{\xi_1,\xi_1,\xi_1,\xi_2,\xi_3\}$	$\{\eta_1,\eta_2,\eta_3,\eta_4,\eta_4\}$
2,1	$\{\xi_1,\xi_1,\xi_2,\xi_3,\xi_4\}$	$\{\eta_1,\eta_1,\eta_1,\eta_2,\eta_3\}$	2,3	$\{\xi_1,\xi_1,\xi_2,\xi_3,\xi_4\}$	$\{\eta_1,\eta_2,\eta_3,\eta_4,\eta_4\}$
3,1	$\{\xi_1,\xi_2,\xi_3,\xi_4,\xi_5\}$	$\{\eta_1,\eta_1,\eta_1,\eta_2,\eta_3\}$	3,3	$\{\xi_1,\xi_2,\xi_3,\xi_4,\xi_5\}$	$\{\eta_1,\eta_2,\eta_3,\eta_4,\eta_4\}$
4,1	$\{\xi_2,\xi_3,\xi_4,\xi_5,\xi_6\}$	$\{\eta_1,\eta_1,\eta_1,\eta_2,\eta_3\}$	4,3	$\{\xi_2,\xi_3,\xi_4,\xi_5,\xi_6\}$	$\{\eta_1,\eta_2,\eta_3,\eta_4,\eta_4\}$
5,1	$\{\xi_3,\xi_4,\xi_5,\xi_6,\xi_6\}$	$\{\eta_1,\eta_1,\eta_1,\eta_2,\eta_3\}$	5,3	$\{\xi_3,\xi_4,\xi_5,\xi_6,\xi_6\}$	$\{\eta_1,\eta_2,\eta_3,\eta_4,\eta_4\}$
6,1	$\{\xi_4,\xi_5,\xi_6,\xi_6,\xi_6\}$	$\{\eta_1,\eta_1,\eta_1,\eta_2,\eta_3\}$	6,3	$\{\xi_4,\xi_5,\xi_6,\xi_6,\xi_6\}$	$\{\eta_1,\eta_2,\eta_3,\eta_4,\eta_4\}$
1,2	$\{\xi_1,\xi_1,\xi_1,\xi_2,\xi_3\}$	$\{\eta_1,\eta_1,\eta_2,\eta_3,\eta_4\}$	1,4	$\{\xi_1,\xi_1,\xi_1,\xi_2,\xi_3\}$	$\{\eta_2,\eta_3,\eta_4,\eta_4,\eta_4\}$
2,2	$\{\xi_1,\xi_1,\xi_2,\xi_3,\xi_4\}$	$\{\eta_1,\eta_1,\eta_2,\eta_3,\eta_4\}$	2,4	$\{\xi_1,\xi_1,\xi_2,\xi_3,\xi_4\}$	$\{\eta_2,\eta_3,\eta_4,\eta_4,\eta_4\}$
3,2	$\{\xi_1,\xi_2,\xi_3,\xi_4,\xi_5\}$	$\{\eta_1,\eta_1,\eta_2,\eta_3,\eta_4\}$	3,4	$\{\xi_1,\xi_2,\xi_3,\xi_4,\xi_5\}$	$\{\eta_2,\eta_3,\eta_4,\eta_4,\eta_4\}$
4,2	$\{\xi_2,\xi_3,\xi_4,\xi_5,\xi_6\}$	$\{\eta_1,\eta_1,\eta_2,\eta_3,\eta_4\}$	4,4	$\{\xi_2,\xi_3,\xi_4,\xi_5,\xi_6\}$	$\{\eta_2,\eta_3,\eta_4,\eta_4,\eta_4\}$
5,2	$\{\xi_3,\xi_4,\xi_5,\xi_6,\xi_6\}$	$\{\eta_1,\eta_1,\eta_2,\eta_3,\eta_4\}$	5,4	$\{\xi_3,\xi_4,\xi_5,\xi_6,\xi_6\}$	$\{\eta_2,\eta_3,\eta_4,\eta_4,\eta_4\}$
6,2	$\{\xi_4,\xi_5,\xi_6,\xi_6,\xi_6\}$	$\{\eta_1,\eta_1,\eta_2,\eta_3,\eta_4\}$	6,4	$\{\xi_4,\xi_5,\xi_6,\xi_6,\xi_6\}$	$\{\eta_2,\eta_3,\eta_4,\eta_4,\eta_4\}$

Table I. T-spline knot vectors for the upper T-spline mesh in Figure 5.

REFERENCES

i,j	$\Xi_{i,j}$	$\mathcal{H}_{i,j}$	i,j	$\Xi_{i,j}$	$\mathcal{H}_{i,j}$
1,1	$\{\xi_1,\xi_1,\xi_1,\xi_2,\xi_3\}$	$\{\eta_1,\eta_1,\eta_1,\eta_2,\eta_3\}$	1,5	$\{\xi_1,\xi_1,\xi_1,\xi_2,\xi_3\}$	$\{\eta_3,\eta_4,\eta_5,\eta_6,\eta_7\}$
2,1	$\{\xi_1,\xi_1,\xi_2,\xi_3,\xi_6\}$	$\{\eta_1,\eta_1,\eta_1,\eta_2,\eta_3\}$	2,5	$\{\xi_1,\xi_1,\xi_2,\xi_3,\xi_4\}$	$\{\eta_3,\eta_4,\eta_5,\eta_6,\eta_7\}$
3,1	$\{\xi_1,\xi_2,\xi_3,\xi_6,\xi_7\}$	$\{\eta_1,\eta_1,\eta_1,\eta_2,\eta_3\}$	3,5	$\{\xi_1,\xi_2,\xi_3,\xi_4,\xi_5\}$	$\{\eta_3,\eta_4,\eta_5,\eta_6,\eta_7\}$
6,1	$\{\xi_2,\xi_3,\xi_6,\xi_7,\xi_8\}$	$\{\eta_1,\eta_1,\eta_1,\eta_2,\eta_3\}$	4,5	$\{\xi_2,\xi_3,\xi_4,\xi_5,\xi_6\}$	$\{\eta_3,\eta_4,\eta_5,\eta_6,\eta_7\}$
7,1	$\{\xi_3,\xi_6,\xi_7,\xi_8,\xi_8\}$	$\{\eta_1,\eta_1,\eta_1,\eta_2,\eta_7\}$	5,5	$\{\xi_3,\xi_4,\xi_5,\xi_6,\xi_7\}$	$\{\eta_3,\eta_4,\eta_5,\eta_6,\eta_7\}$
8,1	$\{\xi_6,\xi_7,\xi_8,\xi_8,\xi_8\}$	$\{\eta_1,\eta_1,\eta_1,\eta_2,\eta_7\}$	6,5	$\{\xi_4,\xi_5,\xi_6,\xi_7,\xi_8\}$	$\{\eta_3,\eta_4,\eta_5,\eta_6,\eta_7\}$
1,2	$\{\xi_1,\xi_1,\xi_1,\xi_2,\xi_3\}$	$\{\eta_1,\eta_1,\eta_2,\eta_3,\eta_4\}$	1,6	$\{\xi_1,\xi_1,\xi_1,\xi_2,\xi_3\}$	$\{\eta_4,\eta_5,\eta_6,\eta_7,\eta_8\}$
2,2	$\{\xi_1,\xi_1,\xi_2,\xi_3,\xi_6\}$	$\{\eta_1,\eta_1,\eta_2,\eta_3,\eta_4\}$	2,6	$\{\xi_1,\xi_1,\xi_2,\xi_3,\xi_4\}$	$\{\eta_4,\eta_5,\eta_6,\eta_7,\eta_8\}$
3,2	$\{\xi_1,\xi_2,\xi_3,\xi_6,\xi_7\}$	$\{\eta_1,\eta_1,\eta_2,\eta_3,\eta_4\}$	3,6	$\{\xi_1,\xi_2,\xi_3,\xi_4,\xi_5\}$	$\{\eta_4,\eta_5,\eta_6,\eta_7,\eta_8\}$
6,2	$\{\xi_2,\xi_3,\xi_6,\xi_7,\xi_8\}$	$\{\eta_1,\eta_1,\eta_2,\eta_3,\eta_4\}$	4,6	$\{\xi_2,\xi_3,\xi_4,\xi_5,\xi_6\}$	$\{\eta_4,\eta_5,\eta_6,\eta_7,\eta_8\}$
7,2	$\{\xi_3,\xi_6,\xi_7,\xi_8,\xi_8\}$	$\{\eta_1,\eta_1,\eta_2,\eta_7,\eta_8\}$	5,6	$\{\xi_3,\xi_4,\xi_5,\xi_6,\xi_7\}$	$\{\eta_4,\eta_5,\eta_6,\eta_7,\eta_8\}$
8,2	$\{\xi_6,\xi_7,\xi_8,\xi_8,\xi_8\}$	$\{\eta_1,\eta_1,\eta_2,\eta_7,\eta_8\}$	6,6	$\{\xi_4,\xi_5,\xi_6,\xi_7,\xi_8\}$	$\{\eta_4,\eta_5,\eta_6,\eta_7,\eta_8\}$
1,3	$\{\xi_1,\xi_1,\xi_1,\xi_2,\xi_3\}$	$\{\eta_1,\eta_2,\eta_3,\eta_4,\eta_5\}$	1,7	$\{\xi_1,\xi_1,\xi_1,\xi_2,\xi_3\}$	$\{\eta_5,\eta_6,\eta_7,\eta_8,\eta_8\}$
2,3	$\{\xi_1,\xi_1,\xi_2,\xi_3,\xi_4\}$	$\{\eta_1,\eta_2,\eta_3,\eta_4,\eta_5\}$	2,7	$\{\xi_1,\xi_1,\xi_2,\xi_3,\xi_6\}$	$\{\eta_5,\eta_6,\eta_7,\eta_8,\eta_8\}$
3,3	$\{\xi_1,\xi_2,\xi_3,\xi_4,\xi_5\}$	$\{\eta_1,\eta_2,\eta_3,\eta_4,\eta_5\}$	3,7	$\{\xi_1,\xi_2,\xi_3,\xi_6,\xi_7\}$	$\{\eta_5,\eta_6,\eta_7,\eta_8,\eta_8\}$
4,3	$\{\xi_2,\xi_3,\xi_4,\xi_5,\xi_6\}$	$\{\eta_1,\eta_2,\eta_3,\eta_4,\eta_5\}$	6,7	$\{\xi_2,\xi_3,\xi_6,\xi_7,\xi_8\}$	$\{\eta_5,\eta_6,\eta_7,\eta_8,\eta_8\}$
5,3	$\{\xi_3,\xi_4,\xi_5,\xi_6,\xi_7\}$	$\{\eta_1,\eta_2,\eta_3,\eta_4,\eta_5\}$	7,7	$\{\xi_3,\xi_6,\xi_7,\xi_8,\xi_8\}$	$\{\eta_1,\eta_2,\eta_7,\eta_8,\eta_8\}$
6,3	$\{\xi_4,\xi_5,\xi_6,\xi_7,\xi_8\}$	$\{\eta_1,\eta_2,\eta_3,\eta_4,\eta_5\}$	8,7	$\{\xi_6,\xi_7,\xi_8,\xi_8,\xi_8\}$	$\{\eta_1,\eta_2,\eta_7,\eta_8,\eta_8\}$
1,4	$\{\xi_1,\xi_1,\xi_1,\xi_2,\xi_3\}$	$\{\eta_2,\eta_3,\eta_4,\eta_5,\eta_6\}$	1,8	$\{\xi_1,\xi_1,\xi_1,\xi_2,\xi_3\}$	$\{\eta_6,\eta_7,\eta_8,\eta_8,\eta_8\}$
2,4	$\{\xi_1,\xi_1,\xi_2,\xi_3,\xi_4\}$	$\{\eta_2,\eta_3,\eta_4,\eta_5,\eta_6\}$	2,8	$\{\xi_1,\xi_1,\xi_2,\xi_3,\xi_6\}$	$\{\eta_6,\eta_7,\eta_8,\eta_8,\eta_8\}$
3,4	$\{\xi_1,\xi_2,\xi_3,\xi_4,\xi_5\}$	$\{\eta_2,\eta_3,\eta_4,\eta_5,\eta_6\}$	3,8	$\{\xi_1,\xi_2,\xi_3,\xi_6,\xi_7\}$	$\{\eta_6,\eta_7,\eta_8,\eta_8,\eta_8\}$
4,4	$\{\xi_2,\xi_3,\xi_4,\xi_5,\xi_6\}$	$\{\eta_2,\eta_3,\eta_4,\eta_5,\eta_6\}$	6,8	$\{\xi_2,\xi_3,\xi_6,\xi_7,\xi_8\}$	$\{\eta_6,\eta_7,\eta_8,\eta_8,\eta_8\}$
5,4	$\{\xi_3,\xi_4,\xi_5,\xi_6,\xi_7\}$	$\{\eta_2,\eta_3,\eta_4,\eta_5,\eta_6\}$	7,8	$\{\xi_3,\xi_6,\xi_7,\xi_8,\xi_8\}$	$\{\eta_2,\eta_7,\eta_8,\eta_8,\eta_8\}$
6,4	$\{\xi_4,\xi_5,\xi_6,\xi_7,\xi_8\}$	$\{\eta_2,\eta_3,\eta_4,\eta_5,\eta_6\}$	8,8	$\{\xi_6,\xi_7,\xi_8,\xi_8,\xi_8\}$	$\{\eta_2,\eta_7,\eta_8,\eta_8,\eta_8\}$

Table II. T-spline knot vectors for the middle T-spline mesh in Figure 5.

1. D. S. Dugdale. Yielding of steel sheets containing slits. *Journal of Mechanics and Physics of Solids*, 8(2):100–104, 1960.
2. G. I. Barenblatt. *Advances in Applied Mechanics*, volume 7, chapter The Mathematical Theory of Equilibrium Cracks in Brittle Fracture, pages 55–129. Elsevier, 1962.
3. A. A. Griffith. The phenomena of rupture and flow in solids. *Philosophical Transactions of the Royal Society of London. Series A*, 221:163–198, 1921.
4. J. G. Rots. Smeared and discrete representations of localized fracture. *International Journal of Fracture*, 51(1):45–59, 1991.
5. J. C. J. Schellekens and R. de Borst. On the numerical integration of interface elements. *International Journal for Numerical Methods in Engineering*, 36:43–43, 1993.
6. G. T. Camacho and M. Ortiz. Computational modelling of impact damage in brittle materials. *International Journal of Solids and Structures*, 33(20–22):2899–2938, 1996.
7. J. C. Simo, J. Oliver, and F. Armero. An analysis of strong discontinuities induced by strain-softening in rate-independent inelastic solids. *Computational Mechanics*, 12(5):277–296, 1993.
8. J. Oliver. Modelling strong discontinuities in solid mechanics via strain softening constitutive equations. part 2: Numerical simulation. *International Journal for Numerical Methods in Engineering*, 39(21):3601–3623, 1996.
9. G. N. Wells and L. J. Sluys. A new method for modelling cohesive cracks using finite elements. *International Journal for Numerical Methods in Engineering*, 50(12):2667–2682, 2001.
10. N. Moës and T. Belytschko. Extended finite element method for cohesive crack growth. *Engineering Fracture Mechanics*, 69(7):813–833, 2002.
11. J. J. C. Remmers, R. de Borst, and A. Needleman. A cohesive segments method for the simulation of crack growth. *Computational mechanics*, 31(1-2):69–77, 2003.

12. T. J. R. Hughes, J. A. Cottrell, and Y. Bazilevs. Isogeometric analysis: CAD, finite elements, NURBS, exact geometry and mesh refinement. *Computer Methods in Applied Mechanics and Engineering*, 194(39–41):4135–4195, 2005.
13. J. A. Cottrell, T. J. R. Hughes, and Y. Bazilevs. *Isogeometric analysis: Towards integration of CAD and FEA*. Wiley, Chichester, 2009.
14. W. A. Wall, M. A. Frenzel, and C. Cyron. Isogeometric structural shape optimization. *Computer Methods in Applied Mechanics and Engineering*, 197(33-40):2976–2988, 2008.
15. T. Elguedj, Y. Bazilevs, V. M. Calo, and T. J. R. Hughes. B-bar and F-bar projection methods for nearly incompressible linear and non-linear elasticity and plasticity using higher-order NURBS elements. *Computer Methods in Applied Mechanics and Engineering*, 197(33-40):2732–2762, 2008.
16. D. F. Rogers. *An introduction to NURBS*. Academic Press, San Diego, 2001.
17. M. G. A. Tijssens, L. J. Sluys, and E. van der Giessen. Simulation of fracture of cementitious composites with explicit modeling of microstructural features. *Engineering Fracture Mechanics*, 68(11):1245–1263, 2001.
18. C. Miehe and E. Gürses. A robust algorithm for configurational-force-driven brittle crack propagation with R-adaptive mesh alignment. *International Journal for Numerical Methods in Engineering*, 72(2):127–155, 2007.
19. M. G. Cox. The numerical evaluation of B-splines. *IMA Journal of Applied Mathematics*, 10(2), 1972.
20. C. de Boor. On calculating with B-splines. *Journal of Approximation Theory*, 6(1):50–62, 1972.
21. L. Piegl and W. Tiller. *The NURBS book*. Springer-Verlag, Berlin, 2 edition, 1997.
22. G. Farin. *Curves and surfaces for CADG*. Academic Press, Inc., 1993.
23. J. A. Cottrell, T. J. R. Hughes, and A. Reali. Studies of refinement and continuity in isogeometric structural analysis. *Computer Methods in Applied Mechanics and Engineering*, 196(41–44):4160–4183, 2007.
24. H. Gómez, V. M. Calo, Y. Bazilevs, and T. J. R. Hughes. Isogeometric analysis of the Cahn-Hilliard phase-field model. *Computer Methods in Applied Mechanics and Engineering*, 197(49-50):4333–4352, 2008.
25. T. J. R. Hughes, A. Reali, and G. Sangalli. Efficient quadrature for NURBS-based isogeometric analysis. *Computer Methods in Applied Mechanics and Engineering*, 199(5-8):301–313, 2010.
26. T. W. Sederberg, J. Zheng, A. Bakenov, and A. Nasri. T-splines and T-NURCCs. *ACM Transactions on Graphics*, 22(3):477–484, 2003.
27. Y. Bazilevs, V. M. Calo, J. A. Cottrell, J. A. Evans, T. J. R. Hughes, S. Lipton, M. A. Scott, and T. W. Sederberg. Isogeometric analysis using T-splines. *Computer Methods in Applied Mechanics and Engineering*, 199(5–8):229–263, 2010.
28. D. J. Benson, Y. Bazilevs, E. De Luycker, M. C. Hsu, M. A. Scott, T. J. R. Hughes, and T. Belytschko. A generalized finite element formulation for arbitrary basis functions: from isogeometric analysis to XFEM. *International Journal for Numerical Methods in Engineering*, In press, 2010.
29. M. J. Borden, M. A. Scott, J. A. Evans, and T. J. R. Hughes. Isogeometric finite element data structures based on Bézier extraction. *International Journal for Numerical Methods in Engineering*, Submitted, 2010.
30. M. Jirásek. Comparative study on finite elements with embedded discontinuities. *Computer Methods in Applied Mechanics and Engineering*, 188(1-3):307–330, 2000.
31. T. W. Sederberg, D. L. Cardon, G. T. Finnigan, N. S. North, J. Zheng, and T. Lyche. T-spline simplification and local refinement. *ACM Transactions on Graphics*, 23(3):276–283, 2004.
32. M. A. Scott, M. J. Borden, and T. J. R. Hughes. Bézier-based isogeometric methods: Formulation. In *Proceedings of the* 10^{th} *US National Congress on Computatinal Mechanics*, 2009.
33. J. J. C. Remmers. *Discontinuities in Materials and Structures*. PhD thesis, Delft University of Technology, 2006.
34. X. P. Xu and A. Needleman. Void nucleation by inclusion debonding in a crystal matrix. *Modelling and Simulation in Materials Science and Engineering*, 1(2):111–132, 1993.
35. C. V. Verhoosel, J. J. C Remmers, and M. A. Gutiérrez. A dissipation-based arc-length method for robust simulation of brittle and ductile failure. *International Journal for Numerical Methods in Engineering*, 77(9):1290–1321, 2009.
36. R. de Borst, J. J. C. Remmers, A. Needleman, and M. A. Abellan. Discrete vs smeared crack models for concrete fracture: bridging the gap. *Mechanics of Cohesive-frictional Materials*, 28(7-8):583–607, 2004.
37. E. Schlangen. *Experimental and Numerical Analysis of Fracture Processes in Concrete*. PhD thesis, Delft University of Technology, 1993.
38. R. de Borst. Computation of post-bifurcation and post-failure behavior of strain-softening solids. *Computers & Structures*, 25(2):211–224, 1987.
39. M. G. D. Geers, R. de Borst, and R. H. J. Peerlings. Damage and crack modeling in single-edge and double-edge notched concrete beams. *Engineering Fracture Mechanics*, 65(2-3):247–261, 2000.

40. G. N. Wells. *Discontinuous modelling of strain localisation and failure.* PhD thesis, Delft University of Technology, 2001.